Enhanced AC/DC optimal power flow via nested distributed optimization for AC/VSC-MTDC hybrid power systems

Li, Haixiao; Vergara, Pedro P.; Dimitrovski, Robert; Du, Hongjin; Lekić, Aleksandra

DOI
10.1016/j.ijepes.2024.110365

Publication date
2025

Document Version
Final published version

Published in
International Journal of Electrical Power and Energy Systems

Electrical Power and Energy Systems 164 (2025) 110365

Contents lists available at ScienceDirect

International Journal of Electrical Power and Energy Systems

journal homepage: www.elsevier.com/locate/ijepes

Enhanced AC/DC optimal power flow via nested distributed optimization for AC/VSC-MTDC hybrid power systems

Haixiao Li [a,b,*], Pedro P. Vergara [a], Robert Dimitrovski [a,c], Hongjin Du [a], Aleksandra Lekić [a]

[a] Faculty of Electrical Engineering, Mathematics & Computer Science, Delft University of Technology, Mekelweg 5, Delft, 2628 CD, Netherlands
[b] School of Electrical and Electronic Engineering, Chongqing University of Technology, No. 69 Hongguang Rd, Chongqing, 400054, China
[c] Electrical System Design, TenneT TSO GmbH, Bernecker Straße 70, Bayreuth, 95448, Germany

ARTICLE INFO

Keywords:
Multi-terminal DC
AC/DC optimal power flow
Nested distributed optimization
Generalized Benders decomposition
Alternating direction method of multipliers

ABSTRACT

The deployment of voltage source converters (VSC) to facilitate flexible interconnections between the AC grid, renewable energy system (RES) and Multi-terminal DC (MTDC) grid is on the rise. However, significant challenges exist in exploiting coordinated operations for such AC/VSC-MTDC hybrid power systems. One of the most critical issues is how to achieve the optimal operation of such wide-area systems involving several power entities with as minimal communication burden as possible. To address this issue, an enhanced AC/DC optimal power flow (OPF) is specifically proposed. Firstly, a mixed-integer convex AC/DC OPF model is explicitly formulated to describe the optimal operation of such hybrid power systems. Subsequently, a nested distributed optimization method with double iteration loops is developed to offer optimal system-wide decision-making through a more "thorough" distributed communication architecture. In the outer iteration, the original AC/DC OPF problem is decomposed into several slave problems (SPs) associated with systems (including the AC grid and RESs) and one master problem (MP) associated with the integrated VSC-MTDC grid. Generalized Benders decomposition (GBD) serves to solve the master and slave problems iteratively. Techniques such as multi-cut generation and asynchronous updating are utilized to upgrade the GBD performance of computation efficiency and address communication delays. In the inner iteration, the master problem is continuously decomposed into multiple sub-MPs associated with individual VSCs. The alternating direction method of multipliers (ADMM) is employed to solve these sub-MPs iteratively. Proximal terms and heuristic approaches are embedded to enable parallel computation and handling of integer variables. Numerical experiment results finally validate the effectiveness of the proposed enhanced AC/DC OPF. The constructed AC/DC OPF model exhibits acceptable accuracy in terms of power flow calculation, and the developed nested distributed optimization method showcases decent convergence rate and solution optimality performances.

1. Introduction

1.1. Background

Renewable energy systems (RESs) have experienced significant growth over the past decades. With notable developments in RESs, an increasing number of high-voltage direct current (HVDC) transmission grids have been constructed and put into operation worldwide for remote power delivery from sending-end RESs to receive-ending alternating current (AC) power grids. HVDC transmission outperforms HVAC transmission grids much in terms of long-distance power capacity [1]. In the preceding period, the application of HVDC transmission was limited because line-commutated converters (LCCs) were predominantly used for interconnection. The most notable drawbacks of LCC-HVDC include the inability to control active and reactive power independently and the risk of commutation failure [2]. Fortunately, *voltage source converter* (VSC)-based HVDC transmission has emerged and addressed the issues mentioned in LCC-HVDC, gradually becoming an alternative HVDC transmission solution. VSCs facilitate seamless interconnection between AC and DC sides, thereby forming a *multi-terminal DC* (MTDC) transmission network. These networks offer distinct advantages in flexibility and reliability for power transmission [3,4].

Optimal power flow (OPF) serves as a powerful tool in power system analysis, providing a popular approach for achieving optimal operation in such *AC/VSC-MTDC hybrid power systems*. Compared to the conventional OPF in purely AC power systems, the complexity of the AC/DC

* Corresponding author at: Faculty of Electrical Engineering, Mathematics & Computer Science, Delft University of Technology, Mekelweg 5, Delft, 2628 CD, Netherlands.
E-mail addresses: haixiaoli.ee@gmail.com (H. Li), a.lekic@tudelft.nl (A. Lekić).

https://doi.org/10.1016/j.ijepes.2024.110365
Received 13 August 2024; Received in revised form 8 October 2024; Accepted 6 November 2024
Available online 30 November 2024

Nomenclature

Abbreviation

ADMM	Alternating direction method of multipliers.
GBD	Generalized Benders decomposition.
MTDC	Multi-terminal DC.
OPF	Optimal power flow.
RES	Renewable energy system.
SOCP	Second-order cone programming.
VSC	Voltage source converter.

Indices and Sets

$(\hat{\bullet})$	The determined optimization variables.
$(\bar{\bullet})/(\underline{\bullet})$	The upper/lower bound of the corresponding optimization variables.
$(\bullet)^{(s)}$	The optimization variables at the sth inner iteration loop.
$(\bullet)^{[v]}$	The optimization variables at the vth outer iteration loop.
$\mathbb{N}/\mathbb{L}$	The node/branch set.
$\mathcal{N}_x$	The total number of elements in the set that x belongs to.
$(*)^{AC}$	The parameters and variables related to the AC grid.
$(*)^{MTDC}$	The parameters and variables related to the MTDC grid.
$(*)^{RES}$	The parameters and variables related to the RES.
$(*)^{VSC}$	The parameters and variables related to the VSC.

Parameters and Variables Related to the AC Grid

θ_{ij}^{AC}	The phase different along branch ij of the AC grid.
g_{ij}^{AC}/b_{ij}^{AC}	The conductance/susceptance in branch ij of the AC grid.
$p_{i,A2V}^{AC}/q_{i,A2V}^{AC}$	The active/reactive power transmission from the AC grid to the VSC at the node i.
$p_{i,D}/q_{i,D}$	The active/reactive power demand at node i of the AC grid.
$p_{i,G}/q_{i,G}$	The active/reactive power generation at node i of the AC grid.
p_{ij}^{AC}/q_{ij}^{AC}	The active/reactive power flow in branch ij of the AC grid.
p_{i}^{AC}/q_{i}^{AC}	The active/reactive power injection at node i of the AC grid.
$s_{i,G}^{AC}$	The apparent power output of the generator at node i of the AC grid.
s_{ij}^{AC}	The apparent power in branch ij of the AC grid.
u_{i}^{AC}	The square of nodal voltage amplitude at node i of the AC grid.
v_{i}^{AC}	The nodal voltage at node i of the AC grid.

Parameters and Variables Related to the RES

$p_{r,R2V}^{RES}/q_{r,R2V}^{RES}$	The active/reactive power transmission from the RES r to the VSC.
p_{r}^{RES}/q_{r}^{RES}	The active/reactive power output of the RES r.
$q_{r,var}^{RES}$	The var compensation of the RES r.
s_{r}^{RES}	The apparent power output of the RES r.
u_{r}^{RES}	The square of output voltage amplitude of the RES r.
v_{r}^{RES}	The output voltage of the RES r.

Parameters and Variables Related to the MTDC Grid

l_{jh}^{MTDC}	The squared current flow in branch jh of the MTDC grid.
p_{j}^{MTDC}	The active power injection at node j of the MTDC grid.
$p_{j,D2V}^{MTDC}$	The active power transmission from the MTDC grid to the VSC at the node j.
p_{jh}^{MTDC}	The active power flow in branch jh of the MTDC grid.
$r_{jh}^{MTDC}/y_{jh}^{MTDC}$	The resistance/conductance in branch jh of the MTDC grid.
u_{j}^{MTDC}	The square of nodal voltage amplitude at node j of the MTDC grid.
v_{j}^{MTDC}	The nodal voltage at node j of the MTDC grid.

Parameters and Variables Related to the VSC

δ_{PWM}^{VSC}	The PWM modulation ratio of the VSC.
θ_{ij}^{VSC}	The phase different along branch ij on the AC side of the VSC.
$G_{ij}^{VSC}/B_{ij}^{VSC}$	The (i,j) element in the real/imaginary part of the nodal admittance matrix on the AC side of the VSC.
i_{c}^{VSC}	The phase current of the VSC.
$k_{j,drp}^{VSC}$	The droop coefficient of the VSC DC droop control.
l_{c}^{VSC}	The square of phase current amplitude of the VSC.
p_{i}^{VSC}/q_{i}^{VSC}	The active/reactive power injection at node i on the AC side of the VSC.
$p_{j,ref}^{VSC}$	The active power reference of the VSC DC droop control.
p_{loss}^{VSC}	The converter loss inside the VSC.
u_{i}^{VSC}	The square of nodal voltage amplitude at node i on the AC side of the VSC.
$u_{j,ref}^{VSC}$	The squared voltage amplitude reference of the VSC DC droop control.
v_{i}^{VSC}	The nodal voltage at node i on the AC side of the VSC.
$v_{s,ref}^{VSC}$	The voltage amplitude reference of the VSC AC voltage control.

OPF problem for AC/VSC-MTDC hybrid power systems is increased in the following aspects.

- The nonlinearity regarding the VSC model increases the considerable nonconvexity in the OPF modeling, adding extra computational burden. The capacity constraint of the VSC depicts a nonconvex region. Converter loss, which contributes significantly to the total system losses, is a quadratic polynomial function of the VSC phase current [5,6]. The local control associated with the VSC also introduces nonlinearity when the control parameters are optimized [7]. Additionally, the voltage magnitude and reactive power on the AC side must be considered, as the operating conditions of the VSCs strongly depend on these parameters.

- Unlike purely AC power systems, which are usually treated as an entirety, the AC/VSC-MTDC hybrid power system is a typical wide-area and multi-entity system. Widely used centralized and all-in-one optimization approaches can impose a considerable communication burden, and the power entities in the hybrid power system also encounter the challenge of excessive data sharing [8]. Developing an optimization method that minimizes centralized communication dependence as much as possible to coordinate the operation of such a hybrid power system is crucial.

To address the challenges mentioned above, we have carried out targeted work regarding *enhanced AC/DC OPF*: An explicit mixed-integer convex AC/DC OPF model for AC/VSC-MTDC hybrid power system is applied. Notably, considering the structural characteristics of the AC/VSC-MTDC hybrid power system and the problem features of the AC/DC OPF model, a novel nested distributed optimization method is developed. This method incorporates improved *generalized Benders decomposition* (GBD) [9] and improved *alternating direction method of multipliers* (ADMM) [10] to enable the distributed problem solving and provide the coordinated decision making for the AC/VSC-MTDC hybrid power system, based on a more "thorough" system decomposition.

1.2. Literature review

AC/DC OPF is a promising technique for scheduling optimal operation of AC and DC interconnected power systems. In terms of power flow accuracy, there is no doubt that the nonconvex OPF model with well-known nonlinear AC and DC power flow is the most favored. [11] employs the model-free evolutionary algorithm to solve such a nonconvex AC/DC OPF model. The essence of this solving approach lies in an exhaustive approach, where searching an optimal population requires repeatedly executing a large number of AC/DC power flow calculations, rendering the entire solving process computationally intensive. The interior-point method (IPM) can be another option [12]. Compared to evolutionary algorithms, IPM offers a distinct advantage in terms of computational speed and the ability to achieve higher-quality optimization solutions. However, IPM is unable to handle optimization problems with integer variables.

Therefore, in order to achieve efficient problem solving, many scholars study various convex relaxations and linear approximations in different variable spaces for AC and DC power flows. [13] proposes the linearized AC power flow model by first-order Taylor series expansion. [14,15] demonstrate that v^2 is better than v as the independent variable and modifies the linearized AC power flow model. [16] uses Laurent series expansion to achieve linearization of DC power flow. [17] considers that $\pm 5\%$ voltage deviation is normally allowed and proposes a linearized DC power flow that reduces the voltage estimation errors with maximum and minimum voltage weighting factors. For most power flow linearization approaches, the guarantee of calculation accuracy greatly depends on the well-defined initial power points. Convex relaxations can be an alternative option to handle the power flow nonlinearities, as they have a more generalized formulation. [18] proposes a semi-definite programming (SDP) technique to relax AC power flow equations. However, convergence failure, numerical accuracy warnings, and memory run-out problems are also reported in OPF with SDP relaxation [19]. Many studies have shifted to the second-order cone programming (SOCP) technique. [20] proposes the SOCP relaxation of AC power flow, where the nonconvexities in AC power flow equations are handled using rotated second-order cone and arctangent function constraints with respect to nodal voltage angles. [21] proposes the SOCP relaxation of the DC power flow, where the nonconvexities in DC power flow equations are handled by imposing the branch power constraints into rotated second-order cone constraints. A systematic work on AC/DC OPF modeling is carried out in [22]. A variety of formulations, from nonlinear to convexified and linearized, are developed. Thanks to these significant progresses, the nonlinear power flow issue of AC/VSC-MTDC hybrid power systems can be effectively addressed. Besides power flow, VSC operation also introduces nonlinearities, such as the expression of power loss is nonlinear with the squared phase current term and the VSC droop control function has the bilinear term regarding DC voltage and droop coefficient. Piecewise convex techniques can be appropriately employed to realize the tight relaxation of the mentioned nonlinear terms [23,24].

In addition to AC/DC OPF modeling, solving AC/DC OPF problems presents another critical challenge. The AC/VSC-MTDC hybrid power system is a typically multi-area interconnected system, making widely used centralized and all-in-one solving approaches unsuitable. On one side, centralized solving needs to rely on the point-to-point centralized communication network that covers the entire system area. The AC/VSC-MTDC hybrid power system features a wide-area system, so centralized solving would impose a significant communication burden. On the other side, the AC/VSC-MTDC hybrid power system involves multiple power entities, including the AC grid, RES, and VSC-MTDC grid. In reality, these power entities are managed by different operators, and their operational data can only be shared to a limited extent.

Hence, the distributed-solving approach has attracted much more attention than the centralized-solving approach. As previously mentioned, the well-known nonconvex OPF model is the best option considering the power flow accuracy. However, distributed nonconvex OPF suffers more challenges than (mixed-integer)convex distributed OPF, especially in convergence rate. Some powerful distributed optimization, such as ADMM [10], analytical target cascading (ATC) [25], primal–dual method of multipliers (PDMM) [26], and GBD [9], which perform well in (mixed-integer)convex optimization problems, cannot strictly guarantee convergence when solving nonconvex optimization problems. In recent times, a groundbreaking work was laid in [27]. The augmented Lagrangian based alternating direction inexact Newton (ALADIN), specifically designed for nonconvex optimization problems, is applied to solve the general AC OPF problems. Subsequently, [28,29] extend the application of ALADIN to the nonconvex AC/DC OPF problems. Although ALADIN excels in distributedly solving nonconvex optimization problems, its scalability is relatively limited as it cannot handle integer variables. In some cases, the introduction of integer variables is unavoidable, such as additionally considering the optimal unit commitment in the AC side and the optimal topology reconfiguration in the VSC-MTDC side [30–32].

From this perspective, developing distributed OPF based on (mixed-integer)convex optimization models would be a better option. In recent developments, [33] uses the Lagrangian relaxation method to achieve the distributed state estimation for the AC/VSC-MTDC hybrid power system. [34] develops an ADMM-based optimization method for the AC/VSC-MTDC hybrid power system to determine smooth operation points. [35] proposes an accelerated ADMM with a predictor–corrector strategy to solve the distributed AC/DC OPF problem with chance constraints. [36] suggests the PDMM method based on a distributed approach for the AC/VSC-MTDC hybrid network to reach a consensual point for the energy negotiation between the AC and DC networks. [32] employed the GBD to solve the AC/DC OPF model considering MTDC network cognizance. [37,38] treat the AC/VSC-MTDC hybrid power system as a hierarchical system, and ATC method is employed to provide flexible system decomposition and coordinate the system operation. Owing to these proposed approaches, the communication costs associated with managing AC/VSC-MTDC hybrid power systems can be effectively reduced. Additionally, only a small amount of data needs to be exchanged between the various power entities at the boundaries. However, in the aforementioned studies, although the AC system (includes the AC grid and RES) are decomposed into independent subsystems, the DC system is still treated as an entirety. In practice, the VSC-MTDC grid, as the transmission segment, can span hundreds of kilometers. Hence, managing the entire VSC-MTDC grid in an all-in-one way still encounters considerable communication challenges. Even though [37,38] continue to decompose the VSC-MTDC grid into VSC and MTDC components, the communicated burden suffered by VSC-MTDC grid is not alleviated adequately.

1.3. Main contributions

According to the literature review, a critical research gap regarding the current studies on AC/DC OPF for AC/VSC-MTDC hybrid power systems is concluded: ***Most studies have focused on the distributed OPF between the AC systems and VSC-MTDC grid, while little studies consider distributed OPF inside VSC-MTDC grid, which is significant for further reducing communication burdens***.

Therefore, distributed solving approaches for AC/DC OPF still have room for improvement to achieve better-coordinated operation of AC/VSC-MTDC hybrid power systems. This paper proposes the enhanced AC/DC OPF for AC/VSC-MTDC hybrid power systems and explores the potential of using a nested distributed optimization method, which has lower communication requirements compared to many existing distributed optimization methods [32–38]. Our work has threefold main contributions:

- A mixed-integer convex AC/DC OPF model is explicitly formulated in this paper. The conventional, highly nonlinear AC and DC power flow in the AC/VSC-MTDC hybrid power system is appropriately handled by convex relaxations and linear approximations. Piecewise relaxation techniques are applied in handling VSC's nonlinear operational constraints and squared current term in converter losses. Particularly, the successive linear approximation [14] is utilized to enhance the accuracy of the system-wide power flow calculations in our constructed AC/DC OPF model.
- Based on the characteristics of the constructed AC/DC OPF model, the nested distributed optimization framework is accordingly proposed. Instead of following the rules of most distributed-solving approaches for decomposing the AC/VSC-MTDC hybrid power system, a more "thorough" decomposition is applied. In addition to decomposing the integrated AC/VSC-MTDC system into the AC system and VSC-MTDC grid, the VSC-MTDC grid is further decomposed into multiple VSC areas. A specific nested distributed optimization method with inner and outer iteration loops is developed for coordinated operation between the AC systems and VSC-MTDC grid, as well as among multiple VSC areas within the VSC-MTDC grid.
- In the outer iteration, GBD, as the classic method for addressing mixed-integer programming problems, is selected. GBD serves to iteratively solve the master problem (related to the VSC-MTDC grid) and slave problems (related to AC systems). Multi-cut generation and asynchronous updating techniques are taken to upgrade the GBD performances on computation efficiency and responses to communication delays. In the inner iteration, the master problem is further decomposed into multiple sub-master problems (associated with VSC areas). ADMM is employed to iteratively solve the multiple sub-master problems. Proximal terms and heuristic approaches are embedded into ADMM, for achieving parallel distributed sub-master problem-solving and handling integer variables.

This paper begins with the mathematical formulation of a mixed-integer convex AC/DC OPF model in Section 2. Subsequently, the decomposed OPF model and the nested distributed optimization method are illustrated in Section 3. Finally, numerical results are presented and discussed in Section 4, followed by conclusions in Section 5.

2. Mixed-integer convex AC/DC OPF model

In this section, the well-known nonlinear AC/DC OPF formulation is transformed into the mixed-integer convex one. The original nonlinear formulation is introduced first, and then the mixed-integer convex formulation with the specific handling approaches is presented.

2.1. AC grid constraints

The well-known nonlinear power flow of the AC grid is formulated below:

$$p_{ij}^{AC} = g_{ij}^{AC}|v_i^{AC}|^2 - |v_i^{AC} \parallel v_j^{AC}|(g_{ij}^{AC}\cos\theta_{ij}^{AC} + b_{ij}^{AC}\sin\theta_{ij}^{AC}), \tag{1a}$$

$$q_{ij}^{AC} = -b_{ij}^{AC}|v_i^{AC}|^2 + |v_i^{AC} \parallel v_j^{AC}|(b_{ij}^{AC}\cos\theta_{ij}^{AC} - g_{ij}^{AC}\sin\theta_{ij}^{AC}), \tag{1b}$$

$$\forall\ i,j \in \mathbb{N}^{AC},\quad \forall (i,j) \in \mathbb{L}^{AC}$$

where Eq. (1) represents the AC branch flow model. Eqs. (1a) and (1b) makes the branch flow model nonlinear, considering $|v_i^{AC}|$, $|v_j^{AC}|$, θ_{ij}^{AC} that are regarded as the variables. We use the successive linearization technique proposed in [14] to handle them, such that:

$$p_{ij}^{AC} = g_{ij}^{AC}u_i^{AC} - g_{ij}^{P,init}\frac{u_i^{AC}+u_j^{AC}}{2} - b_{ij}^{P,init}\left(\theta_{ij}^{AC} - \theta_{ij}^{init}\right) + g_{ij}^{P,init}\frac{v_{ij}^{L,init}}{2}, \tag{2a}$$

$$q_{ij}^{AC} = -b_{ij}^{Q,init}\frac{u_i^{AC}+u_j^{AC}}{2} - b_{ij}^{AC}u_i^{AC} - g_{ij}^{Q,init}\left(\theta_{ij}^{AC} - \theta_{ij}^{init}\right) + b_{ij}^{Q,init}\frac{v_{ij}^{L,init}}{2}, \tag{2b}$$

where Eqs. (2a) and (2b) constitute the linear constraints, involving u_i^{AC}, u_j^{AC}, θ_{ij}^{AC} as the variables. $g_{ij}^{P,init}$, $b_{ij}^{Q,init}$, $g_{ij}^{Q,init}$, $b_{ij}^{Q,init}$, v_{ij}^{init} are the constants, which are related to the initial AC power flow points. Their specific formulation can be found in Appendix A.

The active and reactive power injections for the AC grid can be specifically formulated as:

$$p_i^{AC} = \sum_{(i,j)} p_{ij}^{AC},\quad q_i^{AC} = \sum_{(i,j)} q_{ij}^{AC}, \tag{3a}$$

$$p_i^{AC} = p_{i,G}^{AC} - p_{i,D}^{AC} - p_{i,A2V}^{AC},\quad q_i^{AC} = q_{i,G}^{AC} - q_{i,D}^{AC} - q_{i,A2V}^{AC}, \tag{3b}$$

$$\forall\ i \in \mathbb{N}^{AC}$$

where Eq. (3) indicates that for the AC grid node, the nodal active (resp. reactive) power injection p_i^{AC} (resp. q_i^{AC}) is contributed by the active power generation of the generator $p_{i,G}^{AC}$ (resp. $q_{i,G}^{AC}$), the active (resp. reactive) power demand of the load $p_{i,D}^{AC}$ (resp. $q_{i,D}^{AC}$), and the active (resp. reactive) power transmission $p_{i,A2V}^{AC}$ (resp. $q_{i,A2V}^{AC}$). For the AC grid node, if there is no connection to the generator (resp. the VSC station), then $p_{i,G}^{AC}=0, q_{i,G}^{AC}=0$ (resp. $p_{i,A2V}^{AC}=0, q_{i,A2V}^{AC}=0$).

Additionally, some operational constraints need to be considered, such that:

$$(p_{i,G}^{AC})^2 + (q_{i,G}^{AC})^2 \le (\overline{s_{i,G}^{AC}})^2 \tag{4}$$

$$(p_{ij}^{AC})^2 + (q_{ij}^{AC})^2 \le (\overline{s_{ij}^{AC}})^2 \tag{5}$$

$$\underline{|v_i^{AC}|} \le |v_i^{AC}| \le \overline{|v_i^{AC}|} \tag{6}$$

$$\forall\ i,j \in \mathbb{N}^{AC},\quad \forall (i,j) \in \mathbb{L}^{AC}$$

where Eq. (4) regulates the allowable range for $p_{i,G}^{AC}, q_{i,G}^{AC}$, which are constrained by the generator rated capacity $\overline{s_{i,G}^{AC}}$. Eq. (5) indicates the capacity constraint of the branch flow p_{ij}^{AC}, q_{ij}^{AC}, which are constrained by the branch rated capacity $\overline{s_{ij}^{AC}}$. Eq. (6) indicates the nodal voltage amplitude range of $|v_i^{AC}|$. We can observe that Eqs. (4) and (5) are the nonlinear circular constraints, given $p_{i,G}^{AC}, q_{i,G}^{AC}$ and p_{ij}^{AC}, q_{ij}^{AC} respectively regarded as optimization variables. To handle them, we use n-polygon to approximate the circular constraint [39,40], such that:

$$-\overline{s_{i,G}^{AC}} \le \cos\left(\frac{n\pi}{\mathcal{N}_n}\right)p_{i,G}^{AC} + \sin\left(\frac{n\pi}{\mathcal{N}_n}\right)q_{i,G}^{AC} \le \overline{s_{i,G}^{AC}}, \tag{7a}$$

$$-\overline{s_{ij}^{AC}} \le \cos\left(\frac{n\pi}{\mathcal{N}_n}\right)p_{ij}^{AC} + \sin\left(\frac{n\pi}{\mathcal{N}_n}\right)q_{ij}^{AC} \le \overline{s_{ij}^{AC}}, \tag{7b}$$

$\forall\ n \in \{1, 2, \ldots, \mathcal{N}_n\}$

Besides, to match the squared voltage terms u_i^{AC}, u_j^{AC} in Eq. (2), Eq. (6) is transformed into the squared version, such that:

$$\underline{u_i^{AC}} \le u_i^{AC} \le \overline{u_i^{AC}}. \tag{8}$$

Eventually, Eqs. (2), (3), (7) and (8) constitute the linear constraints to formulate the AC grid operation.

2.2. RES constraints

The RES, e.g., the wind farm or solar station, is considered a PQ-type node. Its internal electrical layout is neglected,[1] with only the point of common coupling (PCC) being reserved. Accordingly, we list simplified fundamental operational constraints, such that:

$$0 \le\ p_r^{RES} \le \overline{p_r^{RES}}, \tag{9}$$

$$(p_r^{RES})^2 + (q_r^{RES})^2 \le (\overline{s_r^{RES}})^2, \tag{10}$$

$$\underline{|v_r^{RES}|} \le |v_r^{RES}| \le \overline{|v_r^{RES}|}, \tag{11}$$

$\forall\ r \in \{1, 2, \ldots, \mathcal{N}_r\}$,

where Eq. (9) regulates the range of the RES active power output p_r^{RES}. The upper bound $\overline{p_r^{RES}}$ is determined by the maximum power point tracking value. RES power outputs p_r^{RES}, q_r^{RES} satisfy the capacity constraint Eq. (10). The upper bound $\overline{s_r^{RES}}$ is determined by the RES rated capacity. Eq. (11) regulates the amplitude range of RES output voltage v_r^{RES}. Similar to Eqs. (4) and (5), Eq. (10) is approximated to a set of linear constraints, such that:

$$-\overline{s_r^{RES}} \le \cos\left(\frac{n\pi}{\mathcal{N}_n}\right) p_r^{RES} + \sin\left(\frac{n\pi}{\mathcal{N}_n}\right) q_r^{RES} \le \overline{s_r^{RES}}, \tag{12}$$

$\forall\ n \in \{1,\ 2,\ \cdots,\ \mathcal{N}_n\}$

Eq. (11) also needs to be transformed into the squared version (the reason will be explained later in Section 2.4), such that:

$$\underline{u_r^{RES}} \le u_r^{RES} \le \overline{u_r^{RES}}. \tag{13}$$

Additionally, the RES is the sending-end system for the AC/MTDC hybrid power system. It is usually equipped with var compensation devices such as STATCOM, which contribute reactive power $q_{r,var}^{RES}$ to support the PCC voltage [43], thus p_r^{RES}, q_r^{RES}, and $q_{r,var}^{RES}$ can be specified as below:

$$p_r^{RES} = p_{r,R2V}^{RES}, \quad q_r^{RES} + q_{r,var}^{RES} = q_{r,R2V}^{RES}, \tag{14a}$$

$$\underline{q_{r,var}^{RES}} \le q_{r,\mathrm{var}}^{RES} \le \overline{q_{r,var}^{RES}}, \tag{14b}$$

$\forall\ r \in \{1,\ 2,\ \cdots,\ \mathcal{N}_r\}$

Eventually, Eqs. (9), (12), (13), and (14) constitute the linear constraints to formulate the RES operation.

2.3. MTDC grid constraints

The well-known nonlinear DC grid power flow is formulated below:

$$p_j^{MTDC} = v_j^{MTDC} \sum_{(j,h)} \left\{ \left(v_j^{MTDC} - v_h^{MTDC} \right) y_{jh}^{MTDC} \right\}, \tag{15}$$

$\forall\ j, h \in \mathbb{N}^{MTDC},\ \ \forall (j,h) \in \mathbb{L}^{MTDC}$

where Eq. (15) represents the DC grid bus flow model. It can be seen that Eq. (15) is nonlinear, given p_j^{MTDC}, v_j^{MTDC}, v_h^{MTDC} regarded as the optimization variables. We use the SOCP-relaxed DC grid power flow proposed in [21] to handle it, such that:

$$p_j^{MTDC} = \sum_{(j,h)} p_{jh}^{MTDC}, \tag{16a}$$

$$p_{jh}^{MTDC} + p_{hj}^{MTDC} = r_{jh}^{MTDC} l_{jh}^{MTDC}, \tag{16b}$$

$$u_j^{MTDC} - u_h^{MTDC} = r_{jh}^{MTDC} \left(p_{jh}^{MTDC} - p_{hj}^{MTDC} \right), \tag{16c}$$

$$p_{jh}^{MTDC} \le\ l_{jh}^{MTDC} u_j^{MTDC}, \tag{16d}$$

where Eq. (16) forms the SOCP-relaxed DC grid power flow by relaxing the inherent equality equation that $p_{jh}^{MTDC} = l_{jh}^{MTDC} u_j^{MTDC}$.

The operational constraints regarding nodal voltage for the MTDC grid is formulated below:

$$\underline{v_j^{MTDC}} \le v_j^{MTDC} \le \overline{v_j^{MTDC}}. \tag{17}$$

$\forall\ j \in \mathbb{N}^{MTDC}$

To match the squared voltage terms u_j^{MTDC}, u_j^{MTDC} in Eqs. (16), (17) is transformed into :

$$\underline{u_j^{MTDC}} \le u_j^{MTDC} \le \overline{u_j^{MTDC}}. \tag{18}$$

Particularly, for the MTDC grid, its each node is connected to one VSC station. Thus, the nodal active power injection p_j^{MTDC} can be specified as:

$$p_j^{MTDC} = -p_{j,D2V}^{MTDC}. \tag{19}$$

$\forall\ j \in \mathbb{N}^{MTDC}$

Eventually, Eqs. (16), (18), and (19) constitute the SOCP-relaxed constraints to formulate the MTDC grid operation.

2.4. VSC constraints

As depicted in Fig. 1, the AC side of the VSC refers to the circuit from PCC bus s to the AC terminal bus c, which is formulated below:

$$p_i^{VSC} = |v_i^{VSC}| \sum_j |v_j^{VSC}| \left(G_{ij}^{VSC} \cos\theta_{ij}^{VSC} + B_{ij}^{VSC} \sin\theta_{ij}^{VSC} \right), \tag{20a}$$

$$q_i^{VSC} = |v_i^{VSC}| \sum_j |v_j^{VSC}| \left(G_{ij}^{VSC} \sin\theta_{ij}^{VSC} - B_{ij}^{VSC} \cos\theta_{ij}^{VSC} \right), \tag{20b}$$

$\forall\ i, j \in \mathbb{N}^{VSC}$

where Eq. (20) represents the AC bus flow model. It is nonlinear, given $|v_i^{VSC}|$, $|v_j^{VSC}|$ and θ_{ij}^{VSC} as the optimization variables. We use the SOCP-relaxed AC grid power flow proposed in [20] to handle them,[2] such that:

$$p_i^{VSC} = \sum_j \left(c_{ii}^{VSC} G_{ij}^{VSC} - s_{ij}^{VSC} B_{ij}^{VSC} \right), \tag{21a}$$

$$q_i^{VSC} = -\sum_j \left(c_{ii}^{VSC} B_{ij}^{VSC} + s_{ij}^{VSC} G_{ij}^{VSC} \right), \tag{21b}$$

$$c_{ij}^{VSC} = c_{ji}^{VSC}, \quad s_{ij}^{VSC} = -s_{ji}^{VSC}, \tag{21c}$$

$$(c_{ij}^{VSC})^2 + (s_{ij}^{VSC})^2 \le\ c_{ii}^{VSC} c_{jj}^{VSC}, \tag{21d}$$

[1] Actually, the large-scale RES features a power collecting system with specific operational constraints involving feeders, renewable energy generators, and other components [41,42]. However, discussing these details is beyond the scope of our work.

[2] SOCP-relaxed AC grid power flow can also be an option to handle Eq. (1). However, commonly used off-the-shelf optimizers might fail to return high-fidelity Lagrangian duals in solving SOCP problems (https://support.gurobi.com/hc/en-us/community/posts/21957674501265-Warning-failed-to-compute-QCP-dual-solution-due-to-inaccurate-barrier-solution), which would affect the application of our developed nested distributed optimization method.

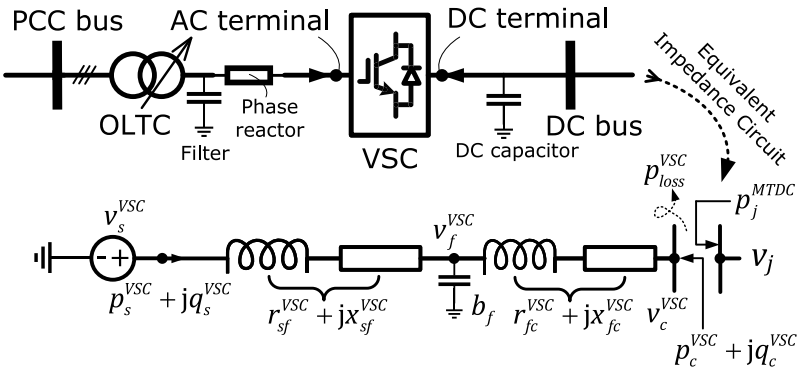

Fig. 1. Equivalent impedance circuit model of the VSC. The circuit covers from the PCC bus to the AC terminal bus.

where Eq. (21) forms the SOCP-relaxed constraints. c_{ii}^{VSC}, c_{ij}^{VSC}, s_{ij}^{VSC} are as the optimization variables, which have links with the nodal voltage amplitude $|v_i^{VSC}|$. Given that $e_i^{VSC} := \Re(v_i^{VSC})$ and $f_i^{VSC} := \Im(v_i^{VSC})$, then the aforementioned optimization variables can be interpreted as $c_{ii}^{VSC} := (e_i^{VSC})^2 + (f_i^{VSC})^2$, $c_{ij}^{VSC} := e_i^{VSC}e_j^{VSC} + f_i^{VSC}f_j^{VSC}$, and $s_{ij}^{VSC} := e_i^{VSC}f_j^{VSC} + e_j^{VSC}f_i^{VSC}$. SOCP-relaxed AC grid power flow is achieved by relaxing the inherent equality equation that $(c_{ij}^{VSC})^2 + (s_{ij}^{VSC})^2 = c_{ii}^{VSC}c_{jj}^{VSC}$.

As depicted in Fig. 1, s is as the boundary node between the AC system (includes the AC grid and RES) and the VSC. Its nodal voltage and power injections can be specifically expressed as:

$$p_s^{VSC} = p_{i,A2V}^{AC} \vee p_{r,R2V}^{RES}, \quad q_s^{VSC} = q_{i,A2V}^{AC} \vee q_{r,R2V}^{RES}, \quad c_{ss}^{VSC} = u_i^{AC} \vee u_r^{RES}, \tag{22}$$

$$\forall\, s \in \mathbb{N}^{VSC}, \quad \forall\, i \in \mathbb{N}^{AC}, \quad \forall\, r \in \{1,\ 2,\ \cdots,\ \mathcal{N}_r\}$$

where Eq. (22) means that if the VSC is connected with the AC grid (resp. the RES), then $p_s^{VSC} = p_{i,A2V}^{AC}$, $q_s^{VSC} = q_{i,A2V}^{AC}$, $c_{ss}^{VSC} = u_i^{AC}$ (resp. $p_s^{VSC} = p_{r,R2V}^{RES}$, $q_s^{VSC} = q_{r,R2V}^{RES}$, $c_{ss}^{VSC} = u_r^{RES}$). Eq. (22) also addresses the previously mentioned question of why Eq. (11) needs to be reformulated as Eq. (13).

A set of constraints are included to characterize the couplings between the VSC's AC terminal and DC terminal, such that:

$$|v_c^{VSC}| = \delta_{PWM}^{VSC} v_j^{MTDC},\ 0 \le \delta_{PWM}^{VSC} \le \overline{\delta_{PWM}^{VSC}}, \tag{23a}$$

$$p_c^{VSC} = p_{j,D2V}^{MTDC} - p_{loss}^{VSC}, \tag{23b}$$

$$p_{loss}^{VSC} = a_{loss,2}|i_c^{VSC}|^2 + a_{loss,1}|i_c^{VSC}| + a_{loss,0}, \tag{23c}$$

$$|i_c^{VSC}v_c^{VSC}|^2 = (p_c^{VSC})^2 + (q_c^{VSC})^2, \quad 0 \le |i_c^{VSC}| \le \overline{|i_c^{VSC}|}, \tag{23d}$$

where Eq. (23) describes the voltage and active power couplings between the VSC's AC terminal and DC terminal. As indicated in Eq. (23a), the PWM modulation factor δ_{PWM}^{VSC} determines the specific voltage coupling. Eq. (23b) represents the active power couplings. The converter loss p_{loss}^{VSC} is generated during the AC/DC power conversion. As indicated in Eq. (23c), the converter loss is a quadratic function with respect to the current amplitude $|i_c^{VSC}|$. $a_{loss,2}$, $a_{loss,1}$, and $a_{loss,0}$ are the corresponding converter loss coefficients. $|i_c^{VSC}|$ can be calculated through Eq. (23d).

Eq. (23) is nonlinear due to: (**a**) The bilinear term $\delta_{PWM}^{VSC} v_j^{MTDC}$ in Eq. (23a). (**b**) The quadratic term $|i_c^{VSC}|^2$ in Eq. (23c). (**c**) The nonlinear equation $|i_c^{VSC}v_c^{VSC}|^2 = (p_c^{VSC})^2 + (q_c^{VSC})^2$ in Eq. (23d). We take three key steps to handle the nonlinearities in Eq. (23): (**i**) The bilinear term $\delta_{PWM}^{VSC} v_j^{MTDC}$ is relaxed into a linear term by eliminating the optimization variable δ_{PWM}^{VSC}, which can be treated as a redundant variable. Besides, to match the squared voltage term c_{ii}^{VSC} in Eq. (21), v_c^{VSC} in (23a) is replaced by c_{cc}^{VSC}. Similarly, to match the squared voltage term u_j^{MTDC} in Eq. (16c), v_j^{MTDC} in Eq. (23a) is replaced by u_j^{MTDC}. (**ii**) Let $l_c^{VSC} = |i_c^{VSC}|^2$, and it is handled by the bivariate piecewise quadratic relaxation [24]. (**iii**) Second-order cone relaxation is taken to handle $|i_c^{VSC}v_c^{VSC}|^2 = (p_c^{VSC})^2 + (q_c^{VSC})^2$. Consequently, Eq. (23) can be transformed into the following mixed-integer convex constraints:

$$c_{cc}^{VSC} \le (\overline{\delta_{PWM}^{VSC}})^2 u_j^{MTDC}, \tag{24a}$$

$$p_c^{VSC} = p_{j,D2V}^{MTDC} - p_{loss}^{VSC}, \tag{24b}$$

$$p_{loss}^{VSC} = a_{loss,2}l_c^{VSC} + a_{loss,1}|i_c^{VSC}| + a_{loss,0}, \tag{24c}$$

$$\left(p_c^{VSC}\right)^2 + \left(q_c^{VSC}\right)^2 \le l_c^{VSC}c_{cc}^{VSC},\ 0 \le |i_c^{VSC}| \le \overline{|i_c^{VSC}|}, \tag{24d}$$

$$l_c^{VSC} \ge \sum_k |i_{c,k}^{VSC}|^2, \tag{24e}$$

$$l_c^{VSC} \le \sum_k \left\{ \overline{|i_{c,k}^{VSC}|}|i_{c,k}^{VSC}| + \underline{|i_{c,k}^{VSC}|}|i_{c,k}^{VSC}| - \overline{|i_{c,k}^{VSC}|}\underline{|i_{c,k}^{VSC}|}b_k \right\}, \tag{24f}$$

$$\sum_k b_k = 1, \quad \sum_k \left|i_{c,k}^{VSC}\right| = \left|i_c^{VSC}\right|, \quad \underline{\left|i_{c,k}^{VSC}\right|}b_k \le \left|i_{c,k}^{VSC}\right| \le \overline{|i_{c,k}|}b_k, \tag{24g}$$

$$\underline{\left|i_{c,k}^{VSC}\right|} = \frac{\overline{|i_c^{VSC}|}(k-1)}{\mathcal{N}_k}, \quad \overline{\left|i_{c,k}^{VSC}\right|} = \frac{\overline{|i_c^{VSC}|}k}{\mathcal{N}_k}, \tag{24h}$$

$$\forall\, k \in \{1, 2\ \cdots\ , \mathcal{N}_k\}$$

where Eq. (24a) is formed by relaxing Eq. (23a), considering that $\delta_{PWM}^{VSC} \ge 0$ and $v_j^{MTDC} \ge 0$. Eq. (24b) keeps consistent with Eq. (23b). Eq. (24c) is reformulated from Eq. (23c), with l_c^{VSC} taking the place of $|i_c^{VSC}|^2$. Eq. (24d) is reformulated from Eq. (23d), by relaxing the inherent formula that $|i_c^{VSC}v_c^{VSC}|^2 = (p_c^{VSC})^2 + (q_c^{VSC})^2$. Eqs. (24e)–(24h) forms the bivariate quadratic envelope to approximate $l_c^{VSC} := |i_c^{VSC}|^2$. $|i_{c,k}^{VSC}|$ denotes the optimization variable within the subrange $\left[\underline{\left|i_{c,k}^{VSC}\right|},\ \overline{\left|i_{c,k}^{VSC}\right|}\right]$, and the binary variable b_k is used to denote the status of each subrange, whether it is enabled (binary-1) or disabled (binary-0).

Furthermore, we consider the impact of VSC vector control on decision making in AC/DC OPF. As shown in Fig. 2, the VSC vector control relies on both outer and inner controllers. The outer controllers include the active and reactive channels. The active channels are responsible for regulating the active power and the DC bus voltage, while the reactive channels are responsible for the reactive power and PCC voltage. For the active channels, droop voltage control is employed for a flexible real-time volt-power response. Specifically, $V^2 - P$ droop control is considered here [44]. The reactive channels use constant AC voltage control benefits in maintaining the output voltage, mainly for RES side [45]. Hence, we have the operational constraints below:

$$c_{ss}^{VSC} = (v_{s,ref}^{VSC})^2, \tag{25}$$

$$p_j^{MTDC} = k_{j,drp}^{MTDC}\left(u_j^{MTDC} - u_{j,ref}^{MTDC}\right) + p_{j,ref}^{MTDC}, \tag{26a}$$

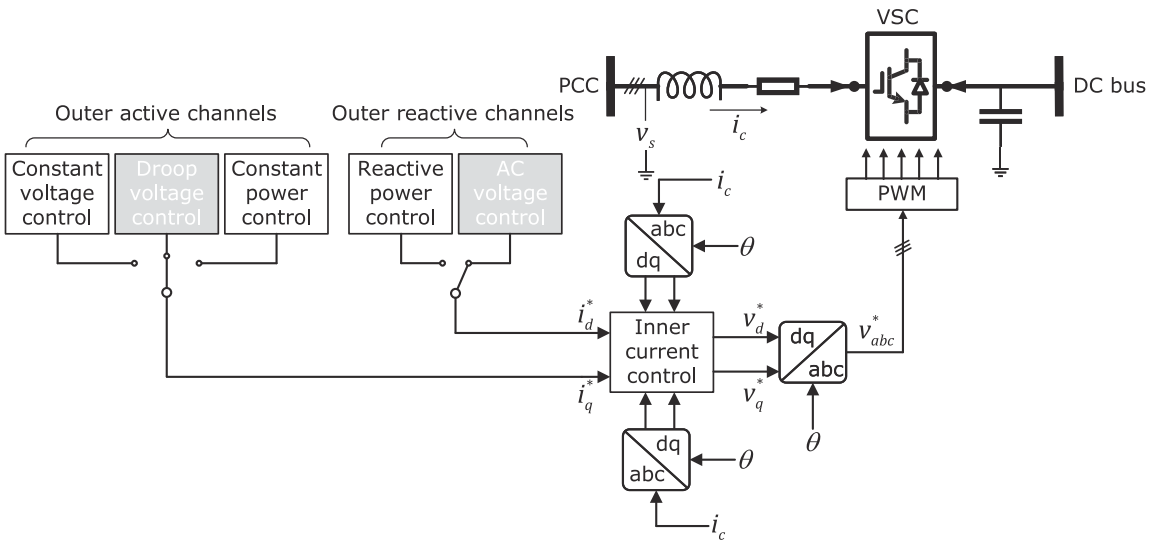

Fig. 2. General architecture of VSC vector control. The outer controllers manage the active and reactive power channels, which are responsible for controlling the AC and DC sides of the VSC, respectively.

$$\underline{k_{j,drp}^{MTDC}} \le k_{j,drp}^{MTDC} \le 0,\ \underline{u_{j}^{MTDC}} \le u_{j,ref}^{MTDC} \le \overline{u_{j}^{MTDC}}, \tag{26b}$$

$$s \in \mathbb{N}^{VSC}, \quad \forall\, j \in \mathbb{N}^{MTDC}$$

where Eq. (25) indicates that the AC voltage amplitude at the PCC bus is imposed to be the reference value $v_{s,ref}^{VSC}$. Eq. (26) formulates the V^2-P droop control function with respect to the power and voltage references $u_{j,ref}^{MTDC}, p_{j,ref}^{MTDC}$.

To improve droop control performance, the droop control parameters $u_{j,ref}^{MTDC}$, $p_{j,ref}^{MTDC}$, $k_{j,drp}^{MTDC}$ are regarded as the optimization variables. In this way, bilinear terms $k_{j,drp}^{MTDC}u_{j}^{MTDC}$ and $k_{j,drp}^{MTDC}u_{j,ref}^{MTDC}$ exist. We handle them using piecewise McCormick envelope [23], e.g., $U_{j,ref}^{MTDC} := k_{j,drp}^{MTDC}u_{j,ref}^{MTDC}$ can be approximated as:

$$U_{j,ref}^{MTDC} \ge \underline{k_{j,drp}^{MTDC}}u_{j,ref}^{MTDC} + \sum_{k}\underline{u_{j,ref,k}^{MTDC}}\Delta k_{j,drp,k}^{MTDC}, \tag{27a}$$

$$U_{j,ref}^{MTDC} \ge \sum_{k}\overline{u_{j,ref,k}^{MTDC}}\left(\Delta k_{j,drp,k}^{MTDC} + \underline{k_{j,drp}^{MTDC}}d_k\right), \tag{27b}$$

$$U_{j,ref}^{MTDC} \le \underline{k_{j,drp}^{MTDC}}u_{j,ref}^{MTDC} + \sum_{k}\overline{u_{j,ref,k}^{MTDC}}\Delta k_{j,drp,k}^{MTDC}, \tag{27c}$$

$$U_{j,ref}^{MTDC} \le \sum_{k}\underline{u_{j,ref,k}^{MTDC}}\left(\Delta k_{j,drp,k}^{MTDC} + \underline{k_{j,drp}^{MTDC}}d_k\right), \tag{27d}$$

$$\underline{u_{j,ref,k}^{MTDC}} = \underline{u_{j,ref}^{MTDC}} + \frac{\left(\overline{u_{j,ref}^{MTDC}} - \underline{u_{j,ref}^{MTDC}}\right)(k-1)}{\mathcal{N}_k}, \tag{27e}$$

$$\overline{u_{j,ref,k}^{MTDC}} = \underline{u_{j,ref}^{MTDC}} + \frac{\left(\overline{u_{j,ref}^{MTDC}} - \underline{u_{j,ref}^{MTDC}}\right)k}{\mathcal{N}_k}, \tag{27f}$$

$$\sum_{k} d_k = 1, \quad k_{j,drp}^{MTDC} = \underline{k_{j,drp}^{MTDC}} + \sum_{k}\Delta k_{j,drp,k}^{MTDC}, \tag{27g}$$

$$\forall\, k \in \{1,2\ \cdots\ ,\mathcal{N}_k\}$$

where the binary variable d_k is enabled (binary-1) for the segment where $U_{j,ref}^{MTDC}$ is located at $\underline{u_{j,ref,k}^{MTDC}} \le U_{j,ref}^{MTDC} \le \overline{u_{j,ref,k}^{MTDC}}$ and is otherwise disabled (binary-0). Eqs. (27a)–(27d) provide a tighter McCormick envelope. Eqs. (27e) and (27f) respectively denote the sub-lower bound and sub-upper bound for $u_{j,ref,k}^{MTDC}$. Eq. (27g) enforces only one binary variable is active. The continuous switch $\Delta k_{j,drp,k}^{MTDC}$ takes on any positive value between 0 and $-k_{j,drp,k}^{MTDC}$ when d_k is enabled at the kth segment. Besides, $U_{j}^{MTDC} := \overline{k_{j,drp}^{MTDC}}u_{j}^{MTDC}$ can be approximated with a set of mixed-integer constraints that are similar to Eqs. (27a)–(27g). Accordingly, Eq. (26a) can be rewritten as a linear equation, such that:

$$p_{j}^{MTDC} - p_{j,ref}^{MTDC} = U_{j}^{MTDC} - U_{j,ref}^{MTDC}. \tag{28}$$

Eventually, Eqs. (21), (22), (24), (25), (27), and (28) compose the mixed-integer convex constraints to formulate the VSC operation.

2.5. Optimization objective for the AC/MTDC hybrid grid

Regarding the optimization objective, minimizing the generation costs and the total power losses (including power losses on lines and inside the VSC station) is considered as the overall optimization objective for the AC/MTDC hybrid power system, such that:

$$\min\left\{\underbrace{\sum_{i}\left(c_{i,2}\left(p_{i,G}^{AC}\right)^2 + c_{i,1}p_{i,G}^{AC} + c_{i,0}\right)}_{\text{generation costs}} + \underbrace{\sum_{i}\left(p_{i,G}^{AC} - p_{i,L}^{AC}\right) + \sum_{r}p_{r}^{RES}}_{\text{total power losses}}\right\}, \tag{29}$$

$$\forall i \in \mathbb{N}^{AC}, \quad \forall r \in \{1,2,\ldots,\mathcal{N}_r\}$$

where the generation costs is a quadratic function with the coefficients $c_{i,2}$, $c_{i,1}$, and $c_{i,0}$. Total power losses include the AC and DC line losses and converter losses, which can be calculated by subtracting the total load demands from the total power generation.

Hence, the enhanced AC/DC OPF model is ultimately formulated as a mixed-integer convex programming problem, specifically, a mixed-integer quadratic programming problem with linear and second-order cone constraints.

3. Nested distributed optimization

The proposed mixed-integer convex AC/DC OPF model is desirable to be solved via a distributed optimization approach, considering communication burdens and privacy protection. In this section, a novel nested distributed optimization framework and the specific distributed optimization methods will be introduced.

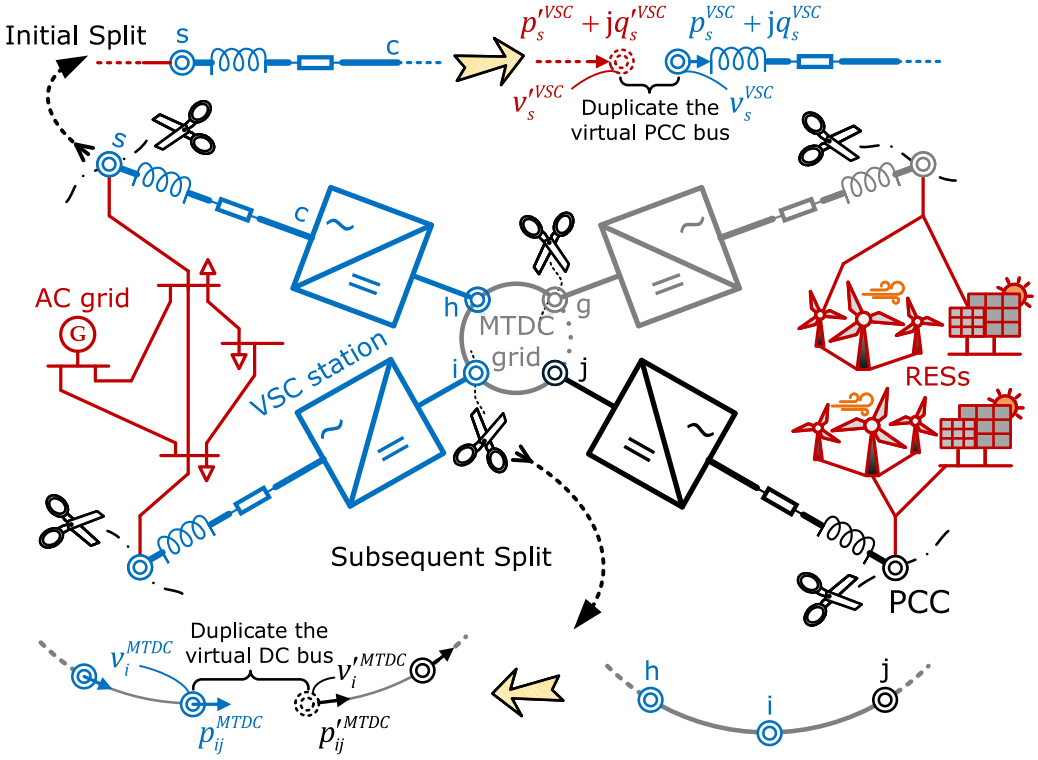

Fig. 3. A schematic of "thorough" system decomposition of the AC/VSC-MTDC hybrid power system. The initial split decomposes the AC system and the VSC-MTDC grid. The subsequent split decomposes the multiple VSC areas inside the VSC-MTDC grid.

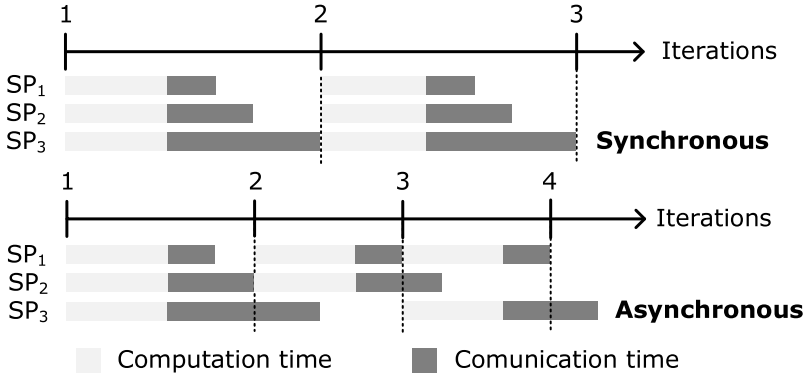

Fig. 4. Illustration regarding the synchronous updating and asynchronous updating. Synchronous updating requires that all SPs must be solved every iteration, while asynchronous updating only requires that a part of SPs must be solved every iteration.

3.1. "Thorough" system decomposition

As shown in Fig. 3, the so-called "thorough" system decomposition involves two stages: The initial split and the subsequent split. Due to data privacy and communication burdens, we deem that different operators govern the AC grid, RES, and MTDC grid separately. The initial split is implemented to address the distributed coordination between the AC system (includes the AC grid and RES system) and VSC-MTDC grid by duplicating the virtual PCC bus and resulting in the additional boundary coupling constraint between the AC systems and the VSC-MTDC grid, such that:

$$p_s^{VSC} = p_s'^{VSC},\ q_s^{VSC} = q_s'^{VSC},\ c_{ss}^{VSC} = c_{ss}'^{VSC}, \tag{30}$$

where $p_s'^{VSC}$, $q_s'^{VSC}$, and $c_{ss}'^{VSC}$ are the duplicated variables at the virtual PCC buses. $c_{ss}^{VSC} = c_{ss}'^{VSC}$ in Eq. (30) is taken replace of the original boundary voltage coupling that $|v_s^{VSC}| = |v_s'^{VSC}|$ to maintain consistent with the squared voltage term in Eq. (21).

Additionally, we consider that the VSC-MTDC grid serves long-distance power transmission, and it usually covers a large geographical area. In the real world, it is highly challenging to establish a global centralized communication network that covers the entire VSC-MTDC grid. Consequently, after the initial split, the VSC-MTDC grid continues to experience subsequent split. Distributed decision making is still needed inside the VSC-MTDC. VSCs connected to an AC grid or a RES system belong to the same VSC area. VSCs located in the same VSC area are geographically closer to each other and are expected to be centrally governed, and distributed coordination is required between the adjacent VSC areas.

The MTDC grid typically exhibits a loop structure, with DC buses numbered clockwise. For the DC bus i, the adjacent buses are the preceding DC bus h and the succeeding bus j. The subsequent split

occurs at the DC bus i by duplicating the virtual DC bus i, resulting in the additional boundary coupling constraint between the DC bus i and DC bus j, such that:

$$p_{ij}^{MTDC} = p_{ij}'^{MTDC},\ u_i^{MTDC} = u_i'^{MTDC}, \tag{31}$$

where $p_{ij}'^{MTDC}$ and $u_i'^{MTDC}$ are the duplicated variables at the virtual DC bus i. $u_i^{MTDC} = u_i'^{MTDC}$ is taken the place of the original boundary voltage coupling that $v_i^{MTDC} = v_i'^{MTDC}$ to maintain consistent with the squared voltage term in Eq. (16). Note that there is no boundary coupling generated between the DC bus i and h because the VSCs connected to them belong to the same VSC area. Similarly, if from the perspective of the DC bus h, there are additional coupling constraints that:

$$p_{gh}'^{MTDC} = p_{gh}^{MTDC},\ u_h'^{MTDC} = u_h^{MTDC}. \tag{32}$$

Based on such "thorough" system decomposition, a set of coupling constraints between the AC systems and the VSC-MTDC grid is generated as the initial split occurs, and a set of coupling constraints between the adjacent VSC areas is generated as the subsequent split occurs.

3.2. Improved GBD in the outer loop with multi-cut generation and asynchronous updating

The constructed AC/DC OPF model is a mixed-integer convex programming problem. Utilizing GBD to achieve distributed optimization between the AC systems and VSC-MTDC grid is highly desirable. The constructed AC/DC OPF model can be formulated in the blow compact formulation:

$$\begin{aligned}
&\min_{\mathbf{X}^{MP},\mathbf{Z}^{MP},\mathbf{X}_m^{SP},\mathbf{Z}_m^{SP}} \sum_m \mathcal{F}_m^{SP}(\mathbf{X}_m^{SP},\mathbf{Z}_m^{SP}),\\
&\text{s.t.}\quad \underbrace{\mathcal{G}^{MP}(\mathbf{X}^{MP},\mathbf{Z}^{MP}) \le 0,\quad \mathcal{H}^{MP}(\mathbf{X}^{MP},\mathbf{Z}^{MP}) = 0,}_{\text{independent constraints in MP}}\\
&\underbrace{\mathcal{G}_m^{SP}(\mathbf{X}_m^{SP},\mathbf{Z}_m^{SP}) \le 0,\quad \mathcal{H}_m^{SP}(\mathbf{X}_m^{SP},\mathbf{Z}_m^{SP}) = 0,}_{\text{independent constraints in SP } m}\\
&\underbrace{\mathcal{H}_m^{CP}(\mathbf{Z}^{MP},\mathbf{Z}_m^{SP}) = 0}_{\text{coupling constraints between MP and SP } m},
\end{aligned} \tag{33}$$

$$\forall m \in \{1,\ 2,\ \cdots,\ \mathcal{N}_m\}$$

where the constructed AC/DC OPF model is decomposed into one master problem (MP) and multiple slave problems (SPs). MP is associated with the VSC-MTDC grid, whereas SPs are associated with the AC systems. $\mathbf{X}^{MP}$ and $\mathbf{X}_m^{SP}$ respectively denote the independent variable vectors only exists in MP and SPs. $\mathbf{Z}^{MP}$ and $\mathbf{Z}_m^{SP}$ respectively the coupling variable vectors associated with MP and SPs. More specifically, MP constraint vectors $\mathcal{G}^{MP}$ and $\mathcal{H}^{MP}$ include Eqs. (16), (18), (19), (21), (22), (24), (25), (27), and (28). SP constraint vectors $\mathcal{G}_m^{SP}$ and $\mathcal{H}_m^{SP}$ include Eqs. (2), (3), (4), (7), (8), (9), (12), (13), and (14). Coupling constraint vectors $\mathcal{H}_m^{CP}$ include Eq. (30). Particularly, we have that:

$$\begin{aligned}
\mathbf{Z}^{MP} &:= \left[p_{s,1}^{VSC}, q_{s,1}^{VSC}, c_{ss,1}^{VSC}, \ldots, p_{s,\mathcal{N}_m}^{VSC}, q_{s,\mathcal{N}_m}^{VSC}, c_{ss,\mathcal{N}_m}^{VSC}\right]^\top,\\
\mathbf{Z}_m^{SP} &:= \left[p_{s,m}'^{VSC}, q_{s,m}'^{VSC}, c_{ss,m}'^{VSC}\right]^\top,
\end{aligned} \tag{34}$$

where $(*)_{s,m}^{VSC}$ is utilized to denote the variables at PCC node s associated with the VSC m. We would like to address that $\mathcal{F}^{MP}$, the optimization objective of MP, should have appeared in Eq. (33). However, reviewing Eq. (29), it can be observed that for our proposed AC/DC OPF model, the optimization objective does not involve the optimization variables in MP associated with the VSC-MTDC grid, i.e., $\mathcal{F}^{MP}(\mathbf{X}^{MP},\mathbf{Z}^{MP}) := \varnothing$.

GBD offers an iterative approach to solve MP and SPs in a distributed manner. Firstly, the SP is formulated as:

$$\begin{aligned}
&\text{Original SP} \triangleq \min_{\mathbf{X}_m^{SP},\mathbf{Z}_m^{SP}} \mathcal{F}_m^{SP}\left(\mathbf{X}_m^{SP},\ \mathbf{Z}_m^{SP}\right),\\
&\text{s.t. } \mathcal{G}_m^{SP}\left(\mathbf{X}_m^{SP},\ \mathbf{Z}_m^{SP}\right) \le 0,\quad \mathcal{H}_m^{SP}\left(\mathbf{X}_m^{SP},\ \mathbf{Z}_m^{SP}\right) = 0,\\
&\qquad \mathcal{H}_m^{CP}\left(\hat{\mathbf{Z}}^{MP[v]},\ \mathbf{Z}_m^{SP}\right) = 0 \quad \big|\quad \lambda_m,
\end{aligned} \tag{35}$$

$$v \in \{1,\ 2,\ \cdots,\ \mathcal{N}_v\}$$

where Eq. (35) defines the original SP. λ_m is the dual multiplier vector corresponding to the coupling constraint vector that $\mathcal{H}_m^{CP} = 0$. Note that $\hat{\mathbf{Z}}^{MP[v]}$ represents the determined boundary variable vector from MP at the vth GBD iteration. The upper bound (UB) of Eq. (33) is calculated by solving Eq. (35). However, Eq. (35) may have no feasible solutions at a certain iteration. In this case, the relaxed SP taking the place of Eq. (35) is formed:

$$\begin{aligned}
&\text{Relaxed SP} \triangleq \min_{\mathbf{X}_m^{SP},\mathbf{Z}_m^{SP}} \left\{\|\boldsymbol{\epsilon}_m\|_1 + \|\boldsymbol{\sigma}_m\|_1\right\},\\
&\text{s.t. } \mathcal{G}_m^{SP}\left(\mathbf{X}_m^{SP},\ \mathbf{Z}_m^{SP}\right) \le 0,\quad \mathcal{H}_m^{SP}\left(\mathbf{X}_m^{SP},\ \mathbf{Z}_m^{SP}\right) = 0,\\
&\qquad \mathcal{H}_m^{CP}\left(\hat{\mathbf{Z}}^{MP[v]},\ \mathbf{Z}_m^{SP}\right) - \boldsymbol{\epsilon}_m \le 0 \quad \big|\quad \boldsymbol{\mu}_m^{\epsilon},\\
&\qquad -\mathcal{H}_m^{CP}\left(\hat{\mathbf{Z}}^{MP[v]},\ \mathbf{Z}_m^{SP}\right) - \boldsymbol{\sigma}_m \le 0 \quad \big|\quad \boldsymbol{\mu}_m^{\sigma},\\
&\qquad \boldsymbol{\epsilon}_m \geqslant 0,\quad \boldsymbol{\sigma}_m \geqslant 0,
\end{aligned} \tag{36}$$

$$v \in \{1,\ 2,\ \cdots,\ \mathcal{N}_v\}$$

where Eq. (36) define the relaxed SP. $\boldsymbol{\epsilon}_m$ and $\boldsymbol{\sigma}_m$ are auxiliary vectors composed of small positive real numbers for relaxing the quality constraint vector that $\mathcal{H}_m^{CP} = 0$. $\boldsymbol{\mu}_m^{\epsilon}$ and $\boldsymbol{\mu}_m^{\sigma}$ are respectively the dual multiplier vectors corresponding to $\mathcal{H}_m^{CP} - \boldsymbol{\epsilon}_m \le 0$ and $-\mathcal{H}_m^{CP} - \boldsymbol{\sigma}_m \le 0$.

Regarding MP formulation, the archival GBD procedure follows the principle of uni-cut generation, such that:

$$\begin{aligned}
&\text{Uni-Cut MP} \triangleq \min_{\mathbf{X}^{MP},\mathbf{Z}^{MP}} \eta,\\
&\text{s.t. } \mathcal{G}^{MP}\left(\mathbf{X}^{MP},\ \mathbf{Z}^{MP}\right) \le \mathbf{0},\quad \mathcal{H}^{MP}\left(\mathbf{X}^{MP},\mathbf{Z}^{MP}\right) = \mathbf{0},\\
&\mathcal{B}^{opt[v]} \oplus \mathcal{B}^{feas[v]},\\
&\mathcal{B}^{opt[v]} := \eta \ge \hat{\mathcal{I}}^{[v]} + \nabla^\top \mathcal{I}\left(\hat{\mathbf{Z}}^{MP[v]}\right)\left(\mathbf{Z}^{MP} - \hat{\mathbf{Z}}^{MP[v]}\right),\\
&\mathcal{B}^{feas[v]} := 0 \ge \hat{\mathcal{J}}^{[v]} + \nabla^\top \mathcal{J}\left(\hat{\mathbf{Z}}^{MP[v]}\right)\left(\mathbf{Z}^{MP} - \hat{\mathbf{Z}}^{MP[v]}\right),\\
&\mathcal{I} := \mathbf{1}^\top \mathcal{F}^{SP} + \lambda^\top \mathcal{H}^{CP},\\
&\mathcal{J} := \boldsymbol{\mu}^{\epsilon\top} \mathcal{H}^{CP} - \boldsymbol{\mu}^{\sigma\top} \mathcal{H}^{CP},\\
&\mathcal{H}^{CP} := \begin{bmatrix} \mathcal{H}_1^{CP} \\ \mathcal{H}_2^{CP} \\ \vdots \\ \mathcal{H}_{\mathcal{N}_m}^{CP} \end{bmatrix},\quad \mathcal{F}^{CP} := \begin{bmatrix} \mathcal{F}_1^{CP} \\ \mathcal{F}_2^{CP} \\ \vdots \\ \mathcal{F}_{\mathcal{N}_m}^{CP} \end{bmatrix},\\
&\lambda := \begin{bmatrix} \lambda_1 \\ \lambda_2 \\ \vdots \\ \lambda_{\mathcal{N}_m} \end{bmatrix},\quad \boldsymbol{\mu}^{\epsilon} := \begin{bmatrix} \boldsymbol{\mu}_1^{\epsilon} \\ \boldsymbol{\mu}_2^{\epsilon} \\ \vdots \\ \boldsymbol{\mu}_{\mathcal{N}_m}^{\epsilon} \end{bmatrix},\quad \boldsymbol{\mu}^{\sigma} := \begin{bmatrix} \boldsymbol{\mu}_1^{\sigma} \\ \boldsymbol{\mu}_2^{\sigma} \\ \vdots \\ \boldsymbol{\mu}_{\mathcal{N}_m}^{\sigma} \end{bmatrix},
\end{aligned} \tag{37}$$

$$v \in \{1,\ 2,\ \cdots,\ \mathcal{N}_v\}$$

where Eq. (37) forms the uni-cut MP. At the vth iteration, if all SPs have feasible solutions, one integrated linear Benders cut $\mathcal{B}^{opt[v]}$ will be returned, which is named Benders optimality cut. Otherwise, as long as arbitrary SP is infeasible, another integrated linear Benders cut $\mathcal{B}^{feas[v]}$ will be returned, which is named Benders feasibility cut. In this case, each SP cannot be independently handled. It means that, in practice, an additional centralized coordinator is required.

To address the above issue and inspired by [46], we utilize the multi-cut generation technique to improve the GBD iteration procedure,

which is formulated below:

$$\begin{aligned}
&\text{Multi-Cut MP} \triangleq \min_{\mathbf{X}^{MP},\mathbf{Z}^{MP}} \sum_m \eta_m,\\
&\text{s.t. } \mathcal{G}^{MP}\left(\mathbf{X}^{MP},\mathbf{Z}^{MP}\right) \le \mathbf{0}, \quad \mathcal{H}^{MP}\left(\mathbf{X}^{MP},\mathbf{Z}^{MP}\right) = \mathbf{0},\\
&\mathcal{B}_m^{opt[v]} \oplus \mathcal{B}_m^{feas[v]},\\
&\mathcal{B}_m^{opt[v]} := \eta_m \ge \hat{\mathcal{L}}_m^{[v]} + \nabla^\top \mathcal{I}_m\left(\mathbf{Z}^{MP} - \hat{\mathbf{Z}}^{MP[v]}\right),\\
&\mathcal{B}_m^{feas[v]} := 0 \ge \hat{\mathcal{J}}_m^{[v]} + \nabla^\top \mathcal{J}_m\left(\mathbf{Z}^{MP} - \hat{\mathbf{Z}}^{MP[v]}\right),\\
&\mathcal{I}_m := \mathcal{F}_m^{SP} + \boldsymbol{\lambda}_m^\top \boldsymbol{\mathcal{H}}_m^{CP},\\
&\mathcal{J}_m := \boldsymbol{\mu}_m^{\epsilon\top} \boldsymbol{\mathcal{H}}_m^{CP} - \boldsymbol{\mu}_m^{\sigma\top} \boldsymbol{\mathcal{H}}_m^{CP},\\
&\forall v \in \{1,\ 2,\ \cdots,\ \mathcal{N}_v\}, \quad \forall m \in \{1,\ 2,\ \cdots,\ \mathcal{N}_m\}
\end{aligned} \tag{38}$$

where Eq. (38) forms the multi-cut MP. At the vth iteration, each SP m would independently return a linear Benders optimality cut $\mathcal{B}_m^{opt[v]}$ or a linear Benders feasibility cut $\mathcal{B}_m^{feas[v]}$. Consequently, multiple Benders cuts are generated every iteration, and SPs can be solved in parallel without the requirement of a centralized coordinator. The lower bound (LB) of Eq. (33) is calculated by solving Eq. (38).

Additionally, communication delays are likely to occur during the parallel solving of SPs. As shown in Fig. 4, affected by different communication delays, the MP is unable to receive all returned Benders cut from the SPs simultaneously. In this case, two kinds of approaches, synchronous updating and asynchronous updating, can be selected to address this issue. The synchronous updating requires waiting for all SPs to return Benders cuts. In this way, the total computation time depends on the "slowest" SP being solved. In contrast, the asynchronous updating only needs at least $m \ge 1$ SPs to finish returning Benders cut. To ensure sufficient freshness, every SP must finish updating at least once every $v \ge 1$ iteration. Regarding the asynchronous updating steps in multi-cut GBD, we denote the set of SPs that finish returning Benders cuts at the vth iteration as $\mathcal{A}^{[v]}$ and the remaining ones as $\mathcal{C}^{[v]}$. Accordingly, $\mathcal{A}^{[v]} \cap \mathcal{C}^{[v]} = \emptyset$, $\mathcal{A}^{[v]} \cup \mathcal{C}^{[v]} = \{1, \ldots, \mathcal{N}_m\}$. Details about the asynchronous updating in multi-cut GBD are specifically presented in Algorithm 1.

Algorithm 1: **A**synchronous updating of **m**ulti-cut GBD (A-MGBD)

Initialize: $v \leftarrow 0$, $\hat{\mathbf{Z}}^{MP[0]}$, $LB^{[0]}$, $UB^{[0]}$
Repeat
  /* SPs Solving */
  for $m \in \{1,\ 2,\ \cdots,\ \mathcal{N}_m\}$ **do in parallel**
    if $m \in C^{[v]}$ **then**
      $\hat{\mathbf{Z}}^{MP[v]}$ keeps unchanged;
    if *Eq. (35) is feasible* **then**
      Obtain $\hat{\mathbf{X}}_m^{SP[v]}$, $\hat{\mathbf{Z}}_m^{SP[v]}$ by solving Eq. (35);
      Generate $\mathcal{B}_m^{opt[v]}$ to MP and update $\mathcal{F}_m^{SP[v]}$;
    else
      Obtain $\hat{\mathbf{X}}_m^{SP[v]}$, $\hat{\mathbf{Z}}_m^{SP[v]}$ by solving Eq. (36);
      Generate $\mathcal{B}_m^{feas[v]}$ to MP and keep $\hat{\mathcal{F}}_m^{SP[v]} \leftarrow \hat{\mathcal{F}}_m^{SP[v-1]}$;
  $UB^{[v]} = \sum_m \hat{\mathcal{F}}_m^{SP[v]}$;
  /* MP Solving */
  while $m \in \mathcal{A}^{[v]}$ *finish returning Benders cuts* **do**
    Add $\mathcal{B}_m^{opt[v]}$ and $\mathcal{B}_m^{feas[v]}$ according to Eq. (38);
    Obtain $\hat{\mathbf{Z}}^{MP[v+1]}$ by solving Eq. (38) and update $\hat{\eta}_m^{[v]}$;
  $LB^{[v]} = \sum_m \hat{\eta}_m^{[v]}$;
  $v + 1 \leftarrow v$;
Until *Gap between LB and UB is small enough*;

3.3. Proximal ADMM in the inner loop with heuristic approaches to handle integer variables

As depicted in Fig. 3, the VSC-MTDC grid can be regarded as the interconnection of several VSC areas. Therefore, the MP related to the VSC-MTDC grid described in Eq. (38), is desirable to be continuously decomposed into several sub-MPs. ADMM is preferable to be employed to offer distributed problem solving. We assume that the sub-MP l is coupled with the SP m. In this case, the augmented Lagrangian function of sub-MP l can be expressed as:

$$\begin{aligned}
&\min_{\widetilde{\mathbf{X}}_l^{MP},\mathbf{Y}_l^{MP+},\mathbf{Y}_l^{MP-},\mathbf{Z}_l^{MP}} \mathcal{L}_{m,l}^{MP[v](s)} := \eta_m + \boldsymbol{\zeta}_{l/l+1}^{(s)\top}\left(\mathbf{Y}_l^{MP+} - \hat{\mathbf{Y}}_{l+1}^{MP-(s+1)}\right) +\\
&\frac{\rho}{2}\left\|\mathbf{Y}_l^{MP+} - \hat{\mathbf{Y}}_{l+1}^{MP-(s+1)}\right\|^2 + \boldsymbol{\zeta}_{l/l-1}^{(s)\top}\left(\mathbf{Y}_l^{MP-} - \hat{\mathbf{Y}}_{l-1}^{MP+(s)}\right)\\
&+ \frac{\rho}{2}\left\|\mathbf{Y}_l^{MP-} - \hat{\mathbf{Y}}_{l-1}^{MP+(s)}\right\|^2,\\
&\text{s.t. } \mathcal{G}_l^{MP}\left(\widetilde{\mathbf{X}}_l^{MP},\mathbf{Y}_l^{MP},\mathbf{Z}_l^{MP}\right) \le \mathbf{0}, \quad \mathcal{H}_l^{MP}\left(\widetilde{\mathbf{X}}_l^{MP},\mathbf{Y}_l^{MP},\mathbf{Z}_l^{MP}\right) = \mathbf{0},\\
&\mathcal{B}_m^{opt[v]} \oplus \mathcal{B}_m^{\text{feas }[v]},\\
&\mathcal{B}_m^{opt[v]} := \eta_m \ge \hat{\mathcal{I}}_m^{[v]} + \nabla^\top \mathcal{I}_m\left(\mathbf{Z}_l^{MP} - \hat{\mathbf{Z}}_l^{MP[v]}\right),\\
&\mathcal{B}_m^{feas[v]} := 0 \ge \hat{\mathcal{J}}_m^{[v]} + \nabla^\top \mathcal{J}_m\left(\mathbf{Z}_l^{MP} - \hat{\mathbf{Z}}_l^{MP[v]}\right),\\
&\mathcal{I}_m := \mathcal{F}_m^{CP} + \boldsymbol{\lambda}_m^\top \mathcal{H}_m^{CP},\\
&\mathcal{J}_m := \boldsymbol{\mu}_m^{\epsilon\top} \mathcal{H}_m^{CP} - \boldsymbol{\mu}_m^{\sigma\top} \mathcal{H}_m^{CP},\\
&\mathbf{X}_l^{MP} := \begin{bmatrix}\widetilde{\mathbf{X}}_l^{MP}\\ \mathbf{Y}_l^{MP}\end{bmatrix}, \quad \mathbf{Y}_l^{MP} := \begin{bmatrix}\mathbf{Y}_l^{MP+}\\ \mathbf{Y}_l^{MP-}\end{bmatrix},\\
&\mathcal{G}^{MP} := \begin{bmatrix}\mathcal{G}_1^{MP}\\ \mathcal{G}_2^{MP}\\ \vdots\\ \mathcal{G}_{\mathcal{N}_l}^{MP}\end{bmatrix}, \quad \mathcal{H}^{MP} := \begin{bmatrix}\mathcal{H}_1^{MP}\\ \mathcal{H}_2^{MP}\\ \vdots\\ \mathcal{H}_{\mathcal{N}_l}^{MP}\end{bmatrix},\\
&\forall v \in \{1,\ 2,\ \cdots,\ \mathcal{N}_v\}, \quad \forall m \in \{1,\ 2,\ \cdots,\ \mathcal{N}_m\} \quad \forall l \in \{1,\ 2,\ \cdots,\ \mathcal{N}_l\}
\end{aligned} \tag{39}$$

where $(*)_l^{MP}$ is utilized to denote the variables related to sub-MP l. $\mathbf{Y}_l^{MP}$ is the part from $\mathbf{X}_l^{MP}$, which denotes the coupling variables at the boundaries between the adjacent VSC areas. $\widetilde{\mathbf{X}}_l^{MP}$ denotes the remaining variables in $\mathbf{X}_l^{MP}$, which are completely independent. Particularly, due to the typical ring topology of the VSC-MTDC grid, each VSC area is adjacent to two other VSC areas. Hence, $\mathbf{Y}_l^{MP}$ can be split into two parts. One set of variables is $\mathbf{Y}_l^{MP+}$, which represents the coupling variables associated with the preceding VSC area. The other set is $\mathbf{Y}_l^{MP+}$, which represents the coupling variables associated with the subsequent VSC area (with the clockwise direction being considered positive).

After MP decomposition, each sub-MP has two additional coupling constraints, as described by Eqs. (31) and (32). Eq. (31) corresponds to the general formulation as $\mathbf{Y}_l^{MP+} - \mathbf{Y}_{l+1}^{MP-} = 0$ and Eq. (32) corresponds to the general formulation as $\mathbf{Y}_l^{MP-} - \mathbf{Y}_{l-1}^{MP+} = 0$. These two additional coupling constraints are relaxed into the optimization objective, forming the augmented Lagrangian function $\mathcal{L}_{m,l}^{MP}$. $\boldsymbol{\zeta}_{l/l+1}$ and $\boldsymbol{\zeta}_{l/l-1}$ are respectively the dual multipliers corresponding to $\mathbf{Y}_l^{MP+} - \mathbf{Y}_{l+1}^{MP-} = 0$ and $\mathbf{Y}_l^{MP-} - \mathbf{Y}_{l-1}^{MP+} = 0$. ρ is utilized to control the weight of the penalty terms $\left\|\mathbf{Y}_l^{MP-} - \mathbf{Y}_{l-1}^{MP+}\right\|^2$ and $\left\|\mathbf{Y}_l^{MP+} - \mathbf{Y}_{l+1}^{MP-}\right\|^2$. Note that $\hat{\mathbf{Y}}_{l+1}^{MP-(s+1)}$ represents the determined boundary variables from the preceding VSC area at the $s+1$th ADMM iteration and $\hat{\mathbf{Y}}_{l-1}^{MP+(s)}$ represents the determined boundary variable vectors from the subsequent VSC area at the sth ADMM iteration. $\boldsymbol{\zeta}_{l/l+1}^{(s)}$ and $\boldsymbol{\zeta}_{l/l-1}^{(s)}$ represents the dual multiplier vectors at the sth ADMM iteration.

Eq. (39) implies that the standard ADMM follows Gauss–Seidel way for problem solving. This procedure is described below:

$$\begin{aligned}
&\text{Standard ADMM} \triangleq\\
&\hat{\mathbf{Y}}_l^{MP+(s+1)}, \hat{\mathbf{Y}}_l^{MP-(s+1)} \Leftarrow \arg\min \mathcal{L}_{m,l}^{MP[v](s)}\\
&\times\left(\hat{\mathbf{Y}}_{l+1}^{MP-(s+1)}, \mathbf{Y}_l^{MP+}, \mathbf{Y}_l^{MP-}, \hat{\mathbf{Y}}_{l-1}^{MP+(s)}, \hat{\boldsymbol{\zeta}}_{l/l+1}^{(s)}, \hat{\boldsymbol{\zeta}}_{l/l-1}^{(s)}\right),\\
&\hat{\boldsymbol{\zeta}}_{l/l+1}^{(s+1)} \Leftarrow \hat{\boldsymbol{\zeta}}_{l/l+1}^{(s)} + \rho\left(\mathbf{Y}_l^{MP(s+1)+} - \mathbf{Y}_{l+1}^{MP(s+1)-}\right),\\
&\hat{\boldsymbol{\zeta}}_{l/l-1}^{(s+1)} \Leftarrow \hat{\boldsymbol{\zeta}}_{l/l-1}^{(s)} + \rho\left(\mathbf{Y}_l^{MP(s+1)+} - \mathbf{Y}_{l+1}^{MP(s+1)-}\right),
\end{aligned} \tag{40}$$

$$\forall v \in \{1,\ 2,\ \cdots,\ \mathcal{N}_v\},\quad \forall m \in \{1,\ 2,\ \cdots,\ \mathcal{N}_m\}$$

$$\forall l \in \{1,\ 2,\ \cdots,\ \mathcal{N}_l\},\quad \forall s \in \{1,\ 2,\ \cdots,\ \mathcal{N}_s\}$$

As indicated in Eq. (40), solving $\mathcal{L}_{m,l}^{MP[v](s)}$ needs $\hat{\mathbf{Y}}_l^{MP+(s+1)}$, which can only be obtained after the former $\mathcal{L}_{m,l-1}^{MP[v](s)}$ has been solved. Similarly, solving the latter $\mathcal{L}_{m,l+1}^{MP[v](s)}$ needs $\hat{\mathbf{Y}}_l^{MP-(s+1)}$, which can only be obtained after $\mathcal{L}_{m,l}^{MP[v](s)}$ has been solved. Apparently, it is not an appropriate distributed problem-solving way in terms of computation costs.

To address this issue, the proximal term [47] can be added, and into $\mathcal{L}_{m,l}^{MP[v](s)}$ in Eq. (39), then we have that:

$$\begin{aligned}
&\min_{\tilde{\mathbf{X}}_l^{MP},\mathbf{Y}_l^{MP+},\mathbf{Y}_l^{MP-},\mathbf{Z}_l^{MP}} \mathcal{L}_{m,l}^{MP[v](s)} := \eta_m + \boldsymbol{\zeta}_{l/l+1}^{(s)\top}\left(\mathbf{Y}_l^{MP+} - \hat{\mathbf{Y}}_{l+1}^{MP-(s)}\right) + \\
&\frac{\rho}{2}\left\|\mathbf{Y}_l^{MP+} - \hat{\mathbf{Y}}_{l+1}^{MP-(s)}\right\|^2 + \boldsymbol{\xi}_{l/l-1}^{(s)\top}\left(\mathbf{Y}_l^{MP-} - \hat{\mathbf{Y}}_{l-1}^{MP+(s)}\right) \\
&\quad + \frac{\rho}{2}\left\|\mathbf{Y}_l^{MP-} - \hat{\mathbf{Y}}_{l-1}^{MP+(s)}\right\|^2 + \\
&\frac{\beta}{2}\left\|\mathbf{Y}_l^{MP+} - \hat{\mathbf{Y}}_l^{MP+(s)}\right\|^2 + \frac{\beta}{2}\left\|\mathbf{Y}_l^{MP-} - \hat{\mathbf{Y}}_l^{MP-(s)}\right\|^2,
\end{aligned} \tag{41}$$

where $\left\|\mathbf{Y}_l^{MP+} - \hat{\mathbf{Y}}_l^{MP+}\right\|^2$ and $\left\|\mathbf{Y}_l^{MP-} - \hat{\mathbf{Y}}_l^{MP-}\right\|^2$ are as the proximal terms. Similarly to ρ, β is the penalty coefficient to adjust the weight of proximal terms. As a result, the serial distributed solving manner described in Eq. (40) is modified to the parallel distributed solving manner, such that:

$$\begin{aligned}
&\text{Proximal ADMM} \triangleq \\
&\hat{\mathbf{Y}}_l^{MP+(s+1)}, \hat{\mathbf{Y}}_l^{MP-(s+1)} \Leftarrow \arg\min \mathcal{L}_{m,l}^{MP[v](s)} \\
&\quad \times \left(\hat{\mathbf{Y}}_{l+1}^{MP-(s)}, \hat{\mathbf{Y}}_l^{MP+(s)}, \mathbf{Y}_l^{MP+},\ \mathbf{Y}_l^{MP-}, \hat{\mathbf{Y}}_l^{MP-s}, \hat{\mathbf{Y}}_{l-1}^{MP+(s)}, \hat{\boldsymbol{\zeta}}_{l/l+1}^{(s)}, \hat{\boldsymbol{\xi}}_{l/l-1}^{(s)}\right), \\
&\hat{\boldsymbol{\zeta}}_{l/l+1}^{(s)} \Leftarrow \hat{\boldsymbol{\zeta}}_{l/l+1}^{(s)} + \rho\left(\mathbf{Y}_l^{MP(s)+} - \mathbf{Y}_{l+1}^{MP(s)-}\right), \\
&\hat{\boldsymbol{\zeta}}_{l/l-1}^{(s+1)} \Leftarrow \hat{\boldsymbol{\zeta}}_{l/l-1}^{(s)} + \rho\left(\mathbf{Y}_l^{MP(s+1)+} - \mathbf{Y}_{l+1}^{MP(s+1)-}\right),
\end{aligned} \tag{42}$$

$$\forall v \in \{1,\ 2,\ \cdots,\ \mathcal{N}_v\},\quad \forall m \in \{1,\ 2,\ \cdots,\ \mathcal{N}_m\}$$

$$\forall l \in \{1,\ 2,\ \cdots,\ \mathcal{N}_l\},\quad \forall s \in \{1,\ 2,\ \cdots,\ \mathcal{N}_s\}$$

where Eq. (42) implies that all $\mathcal{L}_{m,l}^{MP[v](s)}$ can be solved in parallel.

Additionally, there is still an issue that needs to be addressed when applying proximal ADMM to solve Sub-MPs, namely, the involvement of integer variables. Although ADMM has been applied in solving various mixed-integer convex problems [48], its performances are affected to some extent. To tackle this issue, two heuristic approaches [49,50] are considered to be embedded.

Approach I-Alternating Optimization Procedure : [49] proposed an alternating optimization procedure (AOP) to enhance the ADMM performances on handling integer variables. Briefly, AOP relaxes integer variables into continuous variables and reconstructs them in an iterative way, in conjunction with ADMM to achieve distributed optimization. The procedure of solving sub-MPs described in Eq. (42) using proximal-ADMM in combination with AOP is described in Algorithm 2.

Approach II-Penalty Coefficient Changing: [50] indicated that increasing penalty coefficients would force the convergence and feasibility of ADMM. The ADMM with penalty coefficient changing can be interpreted as a greedy algorithm that first steers to the (sub)optimal solutions depending on the dual multipliers and then steers towards feasibility by increasing penalty coefficients. The procedure of solving sub-MPs described in Eq. (42) using proximal-ADMM considering penalty coefficient changing is described in Algorithm 3.

3.4. Remarks

- As indicated in Eq. (42), $\mathcal{L}_{m,l}^{MP[v](s)}$ is related to both the outer GBD iteration marked by $[v]$ and the inner ADMM iteration marked by (s). Specifically, the outer GBD proceeds to the next iteration only when the inner ADMM converges. Therefore, based on the iterative characteristics of the proposed distributed optimization approach, we describe it as "***Nested***" and we illustrate this kind of approach in Fig. 5.
- The stopping criteria for the outer GBD iteration loop is that the upper and lower bounds of the optimization objective tend to be consistent, which is formulated as Eq. (43). The stopping criteria for the inner ADMM iteration loop is set as the residuals of boundary couplings are sufficiently small, which is formulated as Eq. (44). Besides, if the inner iteration number exceeds the maximum number, the inner iteration loop will also terminate.

$$\left|\frac{LB^{[v]} - UB^{[v]}}{UB^{[v]}}\right| \le thr. \tag{43}$$

Algorithm 2: **A**OP **e**mbedded **p**roximal-ADMM (AE-PADMM)

Initialize: $s \leftarrow 0$, $\hat{\mathbf{Y}}_{l+1}^{MP(0)}$, $\hat{\mathbf{Y}}_{l-1}^{MP(0)}$, $\hat{\boldsymbol{\zeta}}_{l/l+1}^{(0)}$, $\hat{\boldsymbol{\xi}}_{l/l-1}^{(0)}$
Relax binary variables b_k in Eq. (24) and d_k in Eq. (27) into continuous;
/* Step I: solve b_k, d_k -relaxed problem */
Repeat
  for $l \in \{1, \ldots, \mathcal{N}_l\}$ **do in parallel**
    Solve Eq. (42) and obtain $\hat{\mathbf{Y}}_l^{MP+(s)}$, $\hat{\mathbf{Y}}_l^{MP-(s)}$;
  Update $\hat{\boldsymbol{\zeta}}_{l/l+1}^{(s)}$, $\hat{\boldsymbol{\xi}}_{l/l-1}^{(s)}$ based on Eq. (42);
  $s \leftarrow s + 1$;
Until *Residuals is small enough*;
$\hat{\mathbf{Y}}_{l+1}^{MP-*} \leftarrow \hat{\mathbf{Y}}_{l+1}^{MP-(s)}$, $\hat{\mathbf{Y}}_{l-1}^{MP+*} \leftarrow \hat{\mathbf{Y}}_{l-1}^{MP+(s)}$,
$\hat{\boldsymbol{\zeta}}_{l/l+1}^{*} \leftarrow \hat{\boldsymbol{\zeta}}_{l/l+1}^{(s)}, \hat{\boldsymbol{\xi}}_{l/l+1}^{*} \leftarrow \hat{\boldsymbol{\xi}}_{l/l+1}^{(s)}$;
/* Step II: solve $\hat{\mathbf{Y}}_{l+1}^{MP-*}, \hat{\mathbf{Y}}_{l-1}^{MP+*}$, $\hat{\boldsymbol{\zeta}}_{l/l+1}^{*}$, $\hat{\boldsymbol{\xi}}_{l/l-1}^{*}$-fixed problem */
DO
  for $l \in \{1, \ldots, \mathcal{N}_l\}$ **do in parallel**
    Solve Eq. (42) and obtain $\hat{\mathbf{Y}}_l^{MP+(s)}$, $\hat{\mathbf{Y}}_l^{MP-(s)}$;
  Update $\hat{\boldsymbol{\zeta}}_{l/l+1}^{(s)}$, $\hat{\boldsymbol{\xi}}_{l/l-1}^{(s)}$ based on Eq. (42);
  if b_k, d_k *unchanged* **then**
    Break;
  $\hat{b}_k^{*} \leftarrow \hat{b}_k^{(s)}$, $\hat{d}_k^{*} \leftarrow \hat{d}_k^{(s)}$;
/* Step III: solve $\hat{b}_k^{*}, \hat{d}_k^{*}$ -fixed problem */
Repeat
  for $l \in \{1, \ldots, \mathcal{N}_l\}$ **do in parallel**
    Solve Eq. (42) and obtain $\hat{\mathbf{Y}}_l^{MP+(s)}$, $\hat{\mathbf{Y}}_l^{MP-(s)}$;
  Update $\hat{\boldsymbol{\zeta}}_{l/l+1}^{(s)}$, $\hat{\boldsymbol{\xi}}_{l/l-1}^{(s)}$ based on Eq. (42);
  $s \leftarrow s + 1$;
Until *Residuals is small enough*;
Goto *Step II*;

Algorithm 3: **P**enalty coefficient **c**hanging **p**roximal-ADMM (PC-PADMM)

Initialize: $s \leftarrow 0$, $\hat{\mathbf{Y}}_{l+1}^{MP(0)}$, $\hat{\mathbf{Y}}_{l-1}^{MP(0)}$, $\hat{\boldsymbol{\zeta}}_{l/l+1}^{(0)}$, $\hat{\boldsymbol{\xi}}_{l/l-1}^{(0)}$
Repeat
  for $l \in \{1, \ldots, \mathcal{N}_l\}$ **do in parallel**
    Solve Eq. (42) and obtain $\hat{\mathbf{Y}}_l^{MP+(s)}$, $\hat{\mathbf{Y}}_l^{MP-(s)}$;
  Update $\hat{\boldsymbol{\zeta}}_{l/l+1}^{(s)}$, $\hat{\boldsymbol{\xi}}_{l/l-1}^{(s)}$ based on Eq. (42);
  $\rho \leftarrow \alpha\rho$; /* Increase penalty coefficients */
  $s \leftarrow s + 1$;
Until *Residuals is small enough*;

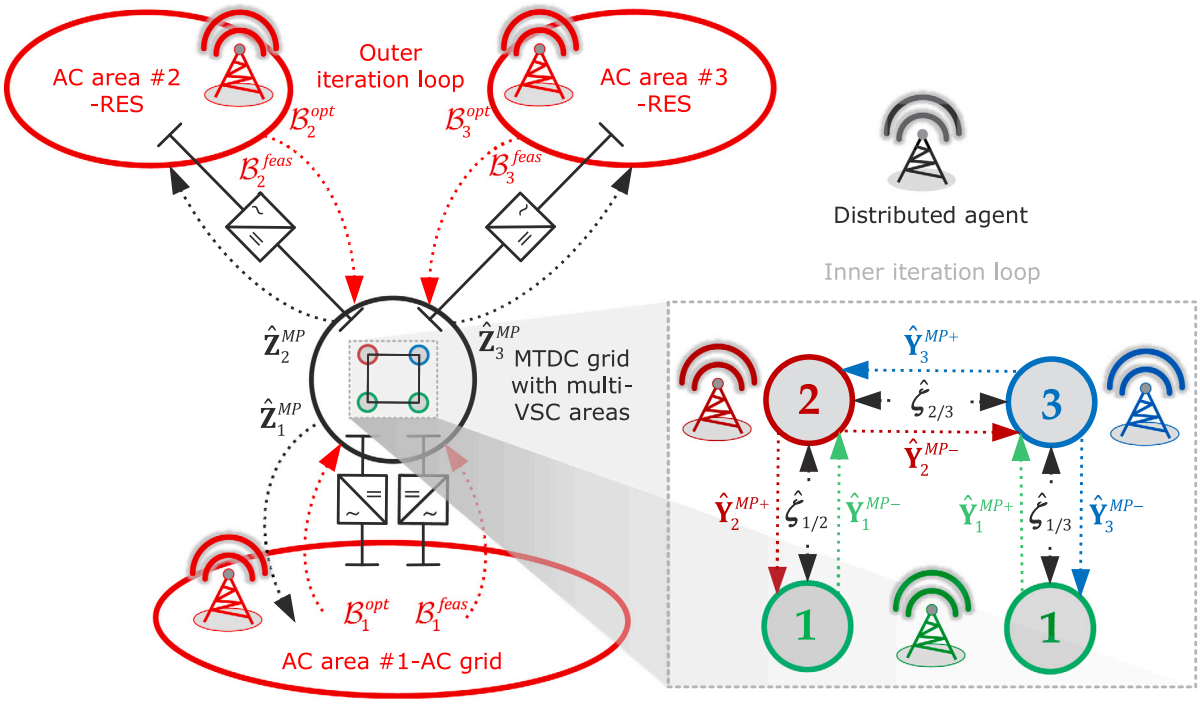

Fig. 5. Illustration regarding the nested distributed optimization. The outer iteration loop is related to the improved GBD and the inner iteration loop is related to the improved ADMM. There are three AC systems including one AC grid and two RESs. Accordingly, the VSC-MTDC area with four terminals needs to be decomposed into three VSC areas according to the number of AC systems.

$$\varepsilon_p^{(s)} := \left\| \begin{matrix} \mathbf{Y}_l^{MP+(s)} - \mathbf{Y}_{l+1}^{MP-(s)} \\ \mathbf{Y}_l^{MP-(s)} - \mathbf{Y}_{l-1}^{MP+(s)} \end{matrix} \right\|_2 \leq thr,$$
$$\varepsilon_d^{(s)} := \rho^{(s)} \cdot \left\| \begin{matrix} \mathbf{Y}_l^{MP+(s)} - \mathbf{Y}_l^{MP+(s-1)} \\ \mathbf{Y}_l^{MP-(s)} - \mathbf{Y}_l^{MP-(s-1)} \end{matrix} \right\|_2 \leq thr. \quad (44)$$

- As indicated Eq. (42), a total of $\mathcal{N}_m$ Benders cuts would be generated in each outer iteration loop, and a total of $\mathcal{N}_l$ sub-MPs would be formulated in each inner iteration loop. Thanks to the system decompose principle illustrated in Section 3.1, we have that $\mathcal{N}_m = \mathcal{N}_l$, which allows multiple Benders cuts to be evenly assigned to each sub-MP. More subtly, the optimization variables contained in one Benders cut exist only in the sub-MP to which they are assigned, but not in any other sub-MPs.
- The accuracy of the linearized AC power flow constraint formulated in Eq. (2) is influenced by the selection of the initial AC power flow points. Furthermore, we deem that the accuracy of the system-wide power flow model for the entire AC/VSC-MTDC hybrid grid is also affected by it. To improve the accuracy of AC/DC power flow, the initial AC power flow points need to be updated appropriately. We extend the power flow point update technique in AC OPF proposed in [14] to our proposed mixed-integer convex AC/DC OPF model for improving the initial AC power flow point setting. The corresponding flow chart is shown in Fig. 6, and the stopping criteria are calculated by the blow normalized errors:

$$\Delta_p = \max\left(\left|\frac{p_n^{k+1} - p_n^k}{p_n^k}\right|\right), \Delta_q = \max\left(\left|\frac{q_n^{k+1} - q_n^k}{q_n^k}\right|\right) \quad (45)$$
$$\forall n \in \mathbb{N}^{AC}$$

  where p_n^k (resp. q_n^k) denotes the nodal active (resp. reactive) power injection value of the AC grid at the kth update.
- There are other combinations for inner and outer distributed optimization methods, such as applying ADMM for the outer iteration loop or GBD for the inner iteration loop, which are also potential options. If ADMM is applied in the outer iteration, it means that ADMM must solve a mixed-integer convex optimization problem in the outer iteration loop. Although some heuristic approaches, such as approaches I and II [49,50] can be used to enhance the performance of ADMM in handling integer variables, a wiser approach is to directly employ optimization algorithms, like GBD, that are designed to solve mixed-integer programming problems. If GBD is applied in the inner iteration, the MP formulated in Eq. (38) needs to be distributedly solved via GBD. However, if we attempt to further decompose the MP into the sub-MP and sub-SPs, we can find that the presence of integer variables in the sub-SPs is unavoidable. In this case, the duals in the sub-SPs cannot be extracted, making GBD inapplicable.

4. Numerical experiment

In this section, we mainly analyze and discuss the accuracy of the constructed mixed-integer convex AC/DC OPF model, the convergence rate of the developed nested distributed optimization method, and the solution optimality regarding the obtained optimization results.

4.1. Simulation setups

We use the test system shown in Fig. 7 as the basic case to validate our constructed mixed-integer convex AC/DC OPF model and the developed nested distributed optimization. The system-wide power flow and voltage are calculated using per-unit value. The voltage bounds in the constructed OPF model are set as $\underline{v_i} := 0.955$p.u., $\overline{v_i} := 1.045$p.u., $\forall i \in \mathbb{N}^{AC} \cup \mathbb{N}^{VSC} \cup \mathbb{N}^{MTDC}$. Considering the potential voltage calculation errors, this voltage bound is more conservative than the normal allowable deviation range of ±0.05p.u.. The default settings for other key boundaries and parameters are: $\overline{s_{i,G}^{AC}} :=$ 1p.u. in Eq. (4), $\overline{s_{ij}^{AC}} :=$ 1.1p.u. in Eq. (5), $\mathcal{N}_n :=$ 16 in Eqs. (7a) and (7b), $\overline{p_r^{RES}} :=$ 0.5p.u in Eq. (10), $\mathcal{N}_n :=$ 16 in Eq. (12), $\overline{q_{r,var}^{RES}} :=$ 0.1p.u, $\underline{q_{r,var}^{RES}} :=$ −0.1p.u in Eq. (14b),

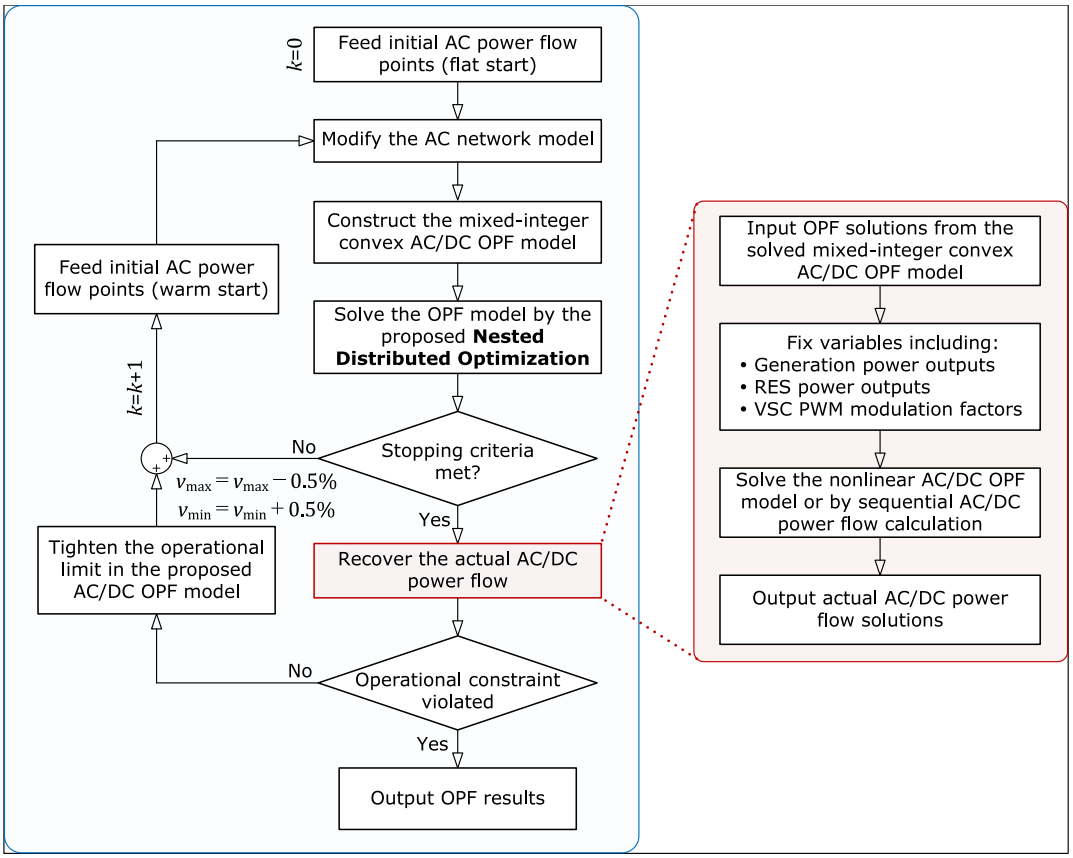

Fig. 6. Flow chart of the successive update regarding the initial AC power flow points in our constructed mixed-integer convex AC/DC OPF model. The update of the initial power flow point begins with the flat start and then changes to the warm start. The AC/DC OPF results should first be checked to see if they satisfy the stopping criteria (formulated in Eq. (45)), which reflects how close the results are to stability. Following that, the AC/DC OPF results are checked for feasibility as the actual AC/DC power flow solutions.

$\overline{\delta_{PWM}^{VSC}}$:= 1.05 in Eq. (23a), $\overline{i_c^{VSC}}$:= 1p.u. in Eq. (24d), $\mathcal{N}_k$:= 6 in Eq. (24h), c_{ss}^{VSC} := 1p.u. in Eq. (25), $k_{j,drp}^{MTDC}$:= −1 in Eqs. (27a) and (27c), $\mathcal{N}_k$:= 2 in Eqs. (27e) and (27f).

The case study is coded on the MATLAB platform. YALMIP toolbox is utilized for the OPF mathematical modeling. During the nested distributed optimization procedure, the GUROBI solver is invoked to solve the constructed mixed-integer convex AC/DC OPF problem. To recover the actual AC/DC power flow, the IPOPT solver is invoked to solve the original nonlinear AC/DC OPF problem and calculate the actual AC/DC power flow solutions. The numerical experiments use a laptop equipped with `12th Gen Intel Core i9 12900HK 2.5 GHz CPU/32 GB RAM`.

4.2. Validation of the constructed AC/DC OPF model

To illustrate the effectiveness of our constructed AC/DC OPF model, we need to validate whether our constructed mixed-integer convex optimization model exhibits acceptable accuracy in AC/DC power flow calculation. We solve our constructed mixed-integer convex AC/DC OPF model and obtain the optimal decision-making regarding $p_{i,G}^{AC}$, $q_{i,G}^{AC}$, $q_{i,G}^{AC}$, p_r^{RES}, q_r^{RES}, $q_{r,var}^{RES}$, δ_{PWM}^{VSC}.[3] Then, we take them into the original nonlinear AC/DC OPF model to obtain the actual system-wide power flow results, which serve as the benchmark. To improve decision quality, we adopted the strategy shown in Fig. 6 to update the initial AC power flow points, and the stop condition is set as $\max(\Delta_p, \Delta_q) < 1 \times 10^{-3}$.

Fig. 8 presents the update process regarding the initial AC power flow points. For the AC grid, its initial AC power flow points are influenced by the injected power at node2 and node5. It can be observed that after 5 updates, the power injections at node2 and node5 converge. During the first and second iterations, the power injections at node2 and node5 have significant fluctuations, indicating that the current power flow points are relatively distant from the initial power flow points. The accuracy of the linear power flow approximation diminishes as the current power flow points further away from the initial power flow points. Fortunately, during the subsequent third to fifth update, the power injection changes become slight, indicating that the current power flow points are close to the initial power flow point, thereby avoiding unacceptable power flow calculation errors.

Fig. 9 further compares the approximated system-wide power flow results from our proposed mixed-integer convex AC/DC OPF model and the actual system-wide power flow results from the well-known nonlinear power flow. It can be found that the maximum absolute value of the relative error in the nodal voltage is less than 0.18%. The errors are acceptable due to the permissible voltage fluctuation of ±0.05 p.u.. On the AC side, the maximum absolute errors of active power and reactive power are about 3.3 MW and 1.8 MVar, respectively. On the DC side, the maximum absolute error of DC power is about 3.2 MW. These errors are acceptable considering the total power demand(apparent) at 100 MVA level.

Moreover, to further validate the acceptability of the proposed OPF model in terms of power flow calculation accuracy and compare the optimization gap between the proposed OPF model and the original nonlinear OPF model, we provide additional numerical experiments based on larger-scale systems. More details can be found in Appendices B and C.

[3] Here, the constructed mixed-integer convex AC/DC OPF model is solved via centralized optimization instead of the nested distributed optimization. This is because we currently focus on validating the model's accuracy rather than the solution's. The interference caused by errors from nested distributed optimization needs to be avoided.

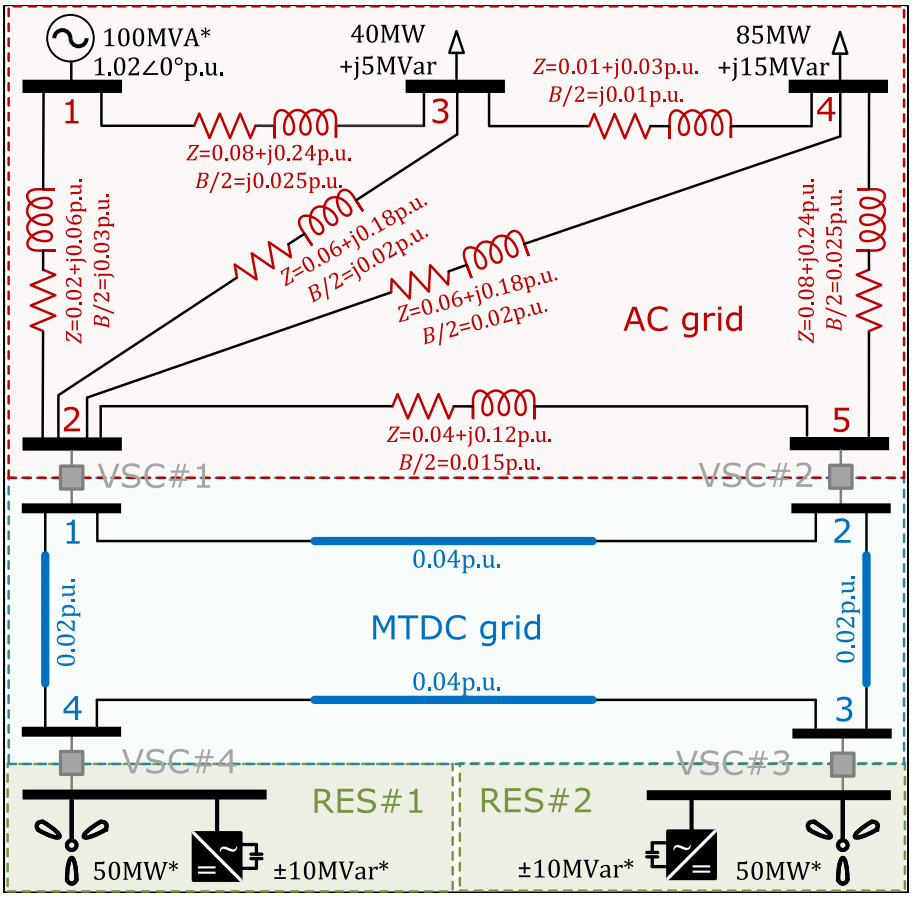

Fig. 7. Schematic diagram of the basic test system, which is composed of one AC grid, two RESs, and four VSCs. The base power and voltage are set to 100 MW and 345 kV. The power marked with $(\bullet)^*$ represents the rated power capacity.

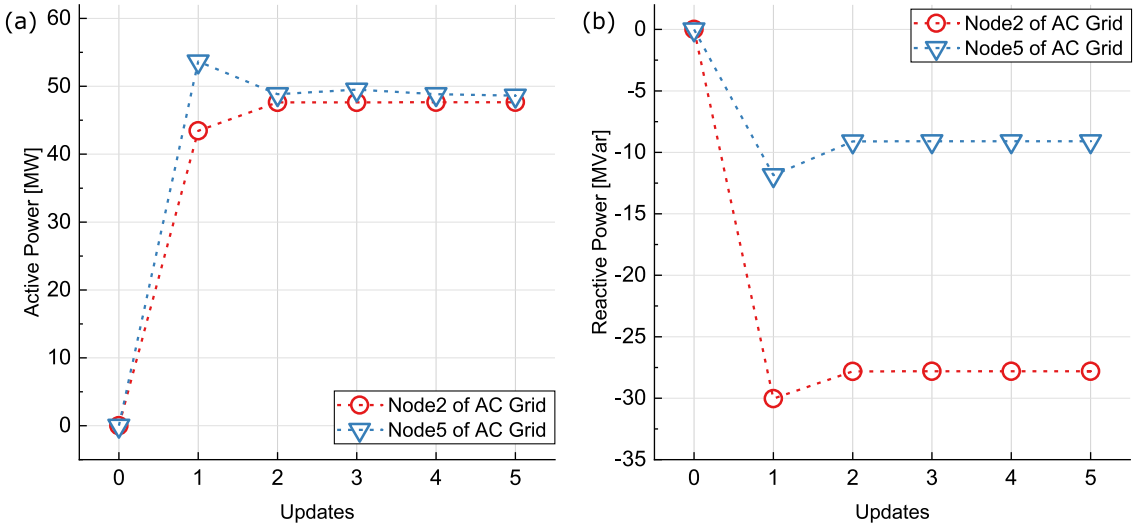

Fig. 8. Update process regarding the AC power flow points, which are influenced by the power injections at node2 and node5 of the AC grid. (a) shows the changes in the active power injection. (b) shows the changes in the reactive power injection.

4.3. Validation of the improved GBD in the outer iteration loop

To illustrate the effectiveness of the improved GBD that involves multi-cut generation and asynchronous updating in the outer iteration loop, we need to validate its convergence rate and solution optimality. When we focus on evaluating the performances regarding distributed problem solving in the outer iteration loop, distributed problem solving in the inner iteration loop would not involved, which means that the MP associated with the VSC-MTDC grid is solved via the centralized way. The threshold in the outer iteration loop is set to 1×10^{-3}. The objective solved via centralized optimization is used as the benchmark.

We first investigate the influence of the multi-cut generation technique on GBD performance. In particular, we set GBD with three kinds of cut generation. **Uni1-GBD** corresponds to the archival GBD

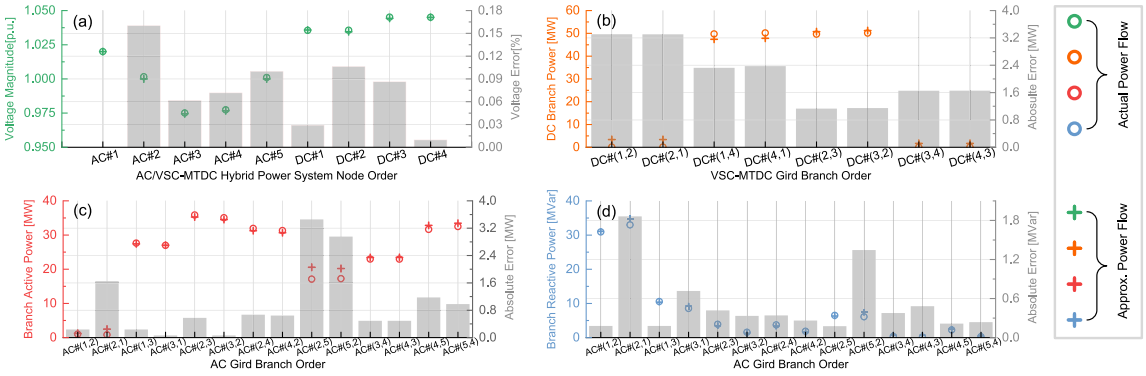

Fig. 9. Comparison of the system-wide approximated and actual power flows. The approximated power flow is based on the proposed mixed-integer convex AC/DC OPF model. The actual power flow is based on the well-known nonlinear AC/DC OPF model. (a) presents the comparison of the nodal voltage calculation. (b) presents the comparison of the DC branch power calculation. (c) and (d) respectively present the comparison of the AC branch active and reactive power calculations.

procedure, and only a single cut is generated per iteration. **Multi2-GBD** corresponds to the multi-cut GBD procedure, and double cuts are generated per iteration. Specifically, SP linked with AC grid generates one cut, SPs linked with RES#1 and RES#2 generate one cut. **Multi3-GBD** also corresponds to the multi-cut GBD procedure, and triple cuts are generated per iteration. Specifically, SPs linked with AC grid, RES#1, and RES#2 generate one cut individually. As presented in Table 1, the objectives in **Uni1-GBD**, **Multi2-GBD**, and **Multi3-GBD** are fairly close to the benchmark and exhibit decent performance in terms of solution optimality. **Multi3-GBD** outperforms **Uni1-GBD** and **Multi2-GBD** in terms of convergence rate. The details regarding the GBD cut generation process are provided in Fig. 10.

We further investigate the influence of the asynchronous updating technology on GBD performance (here, the cut generation approach is applied in **Multi3-GBD**). Particularly, we set four communication scenarios. **Scnr.I** scenario has the perfect communication condition. The standard synchronous updating is adopted. In every iteration, all SPs must have already been solved and returned Benders cuts to MP. **Scnr.II**, **Scnr.III**, **Scnr.IV**, and **Scnr.VI** scenarios have the communication delay conditions. The asynchronous updating described in Algorithm 1 is adopted. For **Scnr.II**, at least two SPs must have already been solved and returned Benders cuts to MP per iteration. The time costs for solving SPs associated with the RES#1, RES#2, and AC grid are assumed to be 2:1:1. For **Scnr.III**, at least two SPs must have already been solved and returned Benders cuts to MP per iteration. The time costs for solving SPs associated with the RES#1, RES#2, and AC grid are assumed to be 3:2:1. For **Scnr.IV**, at least one SP must has already been solved and returned Benders cuts to MP per iteration. The time costs for solving SPs associated with the RES#1, RES#2, and AC grid are assumed to be 3:2:1. For **Scnr.V**, at least two SPs must have already been solved and returned Benders cuts to MP per iteration. The time costs for solving SPs associated with the RES#1, RES#2, and AC grid are assumed to be 4:2:1. For **Scnr.VI**, at least one SP has already been solved and returned Benders cuts to MP per iteration. The time costs for solving SPs associated with the RES#1, RES#2, and AC grid are assumed to be 4:2:1.

Fig. 11 presents the GBD iteration process under the above communication scenarios. In general, compared with synchronous updating, asynchronous updating needs more iterations to converge. This is logical because, under asynchronous updating, MP only accepts partial Benders cuts in each iteration. Therefore, more iterations are needed to receive enough Benders cuts. Table 2 compares the time costs between asynchronous updating and synchronous updating. For most communication scenarios, asynchronous updating is more time-saving because each iteration consumes less time. However, due to the increased number of iterations, the time consumed by asynchronous updating also might be greater than synchronous updating, as seen in **Scnr.V**. Moreover, the converged optimization objectives under all scenarios are still fairly close to the benchmark, which indicates that the improved GBD with multi-cut generation and asynchronous updating still excels in achieving solution optimality.

Table 1
Comparison of GBD with different cut generation.

Description	Iter.	Obj.	Relative Err.
Cen.	–	1.7198	–
Uni1-GBD	17	1.7200	0.0116%
Multi2-GBD	16	1.7201	0.0174%
Multi3-GBD	9	1.7201	0.0174%

Table 2
Comparison of time costs between asynchronous updating and synchronous updating.

Communication scenarios	Time costs (Asyn.:Syn.)
II	0.8333
III	0.7407
IV	0.5926
V	1.7222
VI	0.5556

4.4. Validation of the improved ADMM in the inner iteration loop

To illustrate the effectiveness of the improved ADMM in the outer iteration loop, we need to validate its convergence rate and solution optimality. When we focus on evaluating the performances regarding distributed problem solving in the inner iteration loop, distributed problem solving in the outer iteration loop would not involved, which means the boundary variables of SPs associated with the AC grid, RES#1, and RES#2 are assumed to be constants. In the inner iteration loop, the threshold is set to 1×10^{-3} and the maximum iteration number is set to 250. The objective solved via centralized optimization is used as the benchmark.

We mainly investigate how proximal terms and heuristic approaches influence the ADMM performance on distributed problem solving. We compare the standard ADMM (**SADMM**), ADMM with proximal terms (**PADMM**), **AE-PADMM** (as described in Algorithm 2), and **PC-PADMM** (as described in Algorithm 3). For a fair comparison, the voltage and power terms in the duplicated primary variables are respectively set to 1 p.u. and 0 p.u. Lagrangian duals start from 2, and penalty coefficients are set to 3. The mentioned settings are consistent across all types of ADMM. Particularly, we select the iteration process corresponding to the 6th and 8th outer iteration to present. From Tables 3 and 4, we can see that **SADMM** needs the least iterations to converge. However, the archival iteration procedure in **SADMM** is in serial, which affects the computation efficiency heavily in practice. We can assume that the computation time for each distributed agent equals

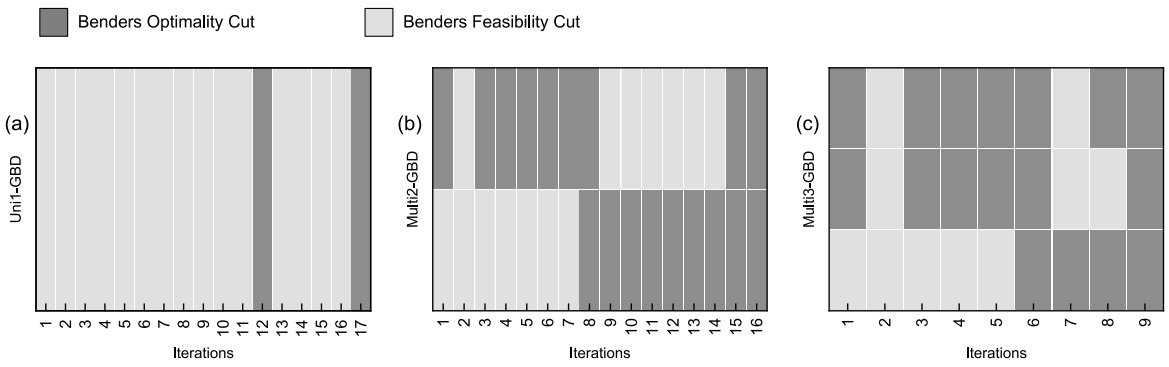

Fig. 10. Details regarding GBD cut generation process. (a) corresponds to Uni1-GBD and only single cut is generated per iteration. (b) and (c) respectively correspond to Multi2-GBD and Multi3-GBD, and multiple cuts are generated per iteration for the both.

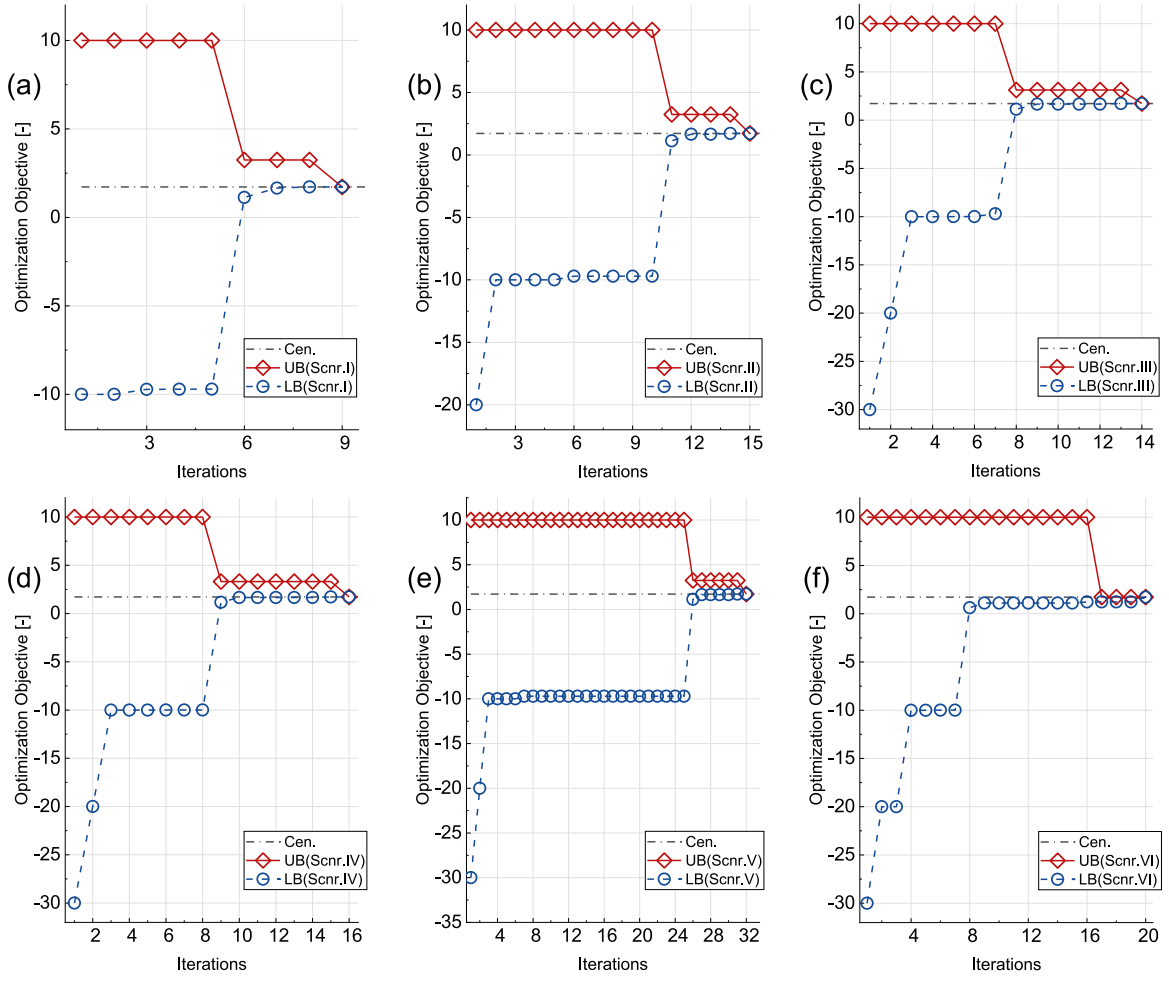

Fig. 11. GBD iteration process under the different communication scenarios. (a) corresponds to the scenario with perfect communication, and synchronous updating is taken. (b)–(e) correspond to the scenario with communication delay, and asynchronous updating is taken.

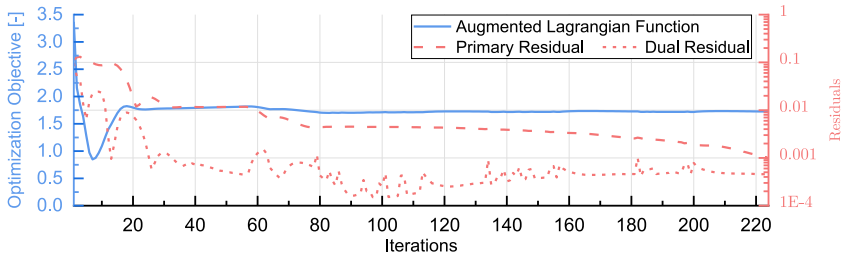

Fig. 12. Inner iteration process at the last outer iteration. PC-PADMM is utilized for problem solving and converge successfully.

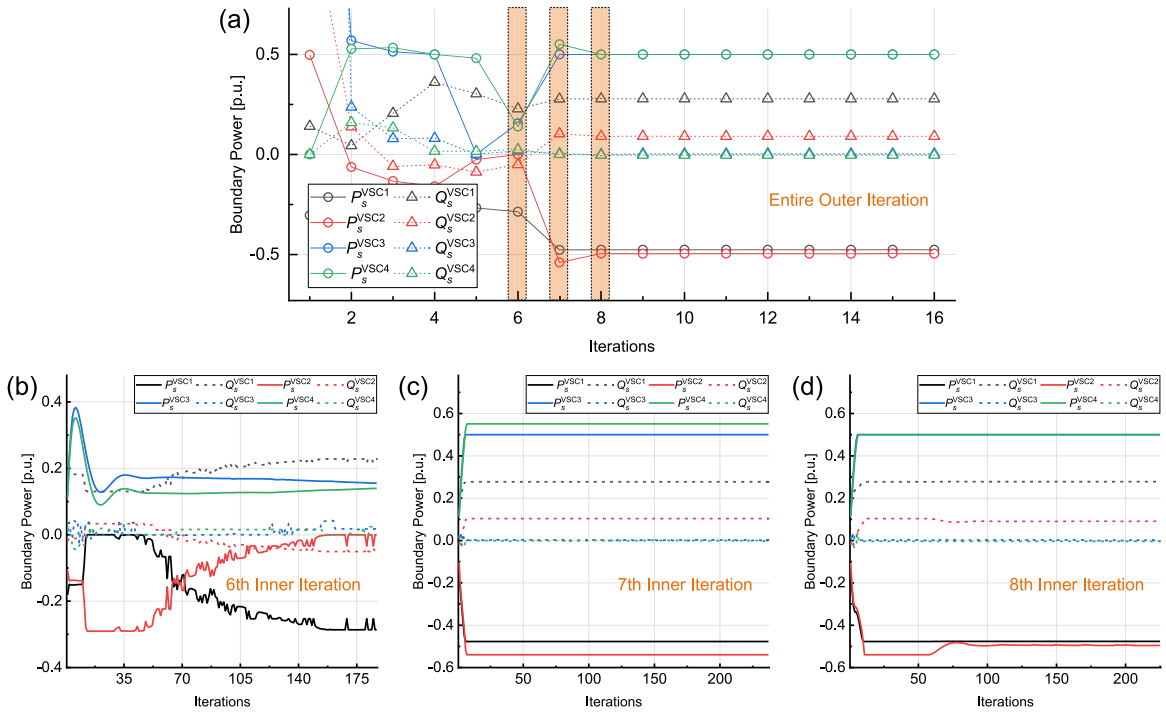

Fig. 13. Changes of boundary power at the PCC bus of VSC, during the outer and inner iteration loops. (a) shows the change during the outer iteration loop. (b), (c), and (d) show the changes during the inner iteration loops, at the 6th, 7th, and 8th outer iteration, respectively.

Table 3
Comparison of different types of ADMM (in the 6th outer iteration).

Description	Iter.	Obj.	Abs. Relative Err.
Cen.	–	1.1316	–
SADMM	154	1.1301	0.1326%
PADMM	208	1.1375	0.5214%
AE-PADMM	429	1.1338	0.1944%
PC-ADMM	225	1.1363	0.4153%

Table 4
Comparison of different types of ADMM (in the 8th outer iteration).

Description	Iter.	Obj.	Abs. Relative Err.
Cen.	–	1.7182	–
SADMM	90	1.7243	0.3550%
PADMM	205	1.7262	0.4656%
AE-PADMM	430	1.7160	0.1280%
PC-ADMM	227	1.7133	0.2852%

$\mathcal{T}$. According to the results in Table 3, the total computation time for **AE-PADMM** with the most iterations would be $429\mathcal{T}$, but the total computation time for **SADMM** with the least iterations would be $616\mathcal{T}(154 \times 4\mathcal{T})$. **PADMM** has fewer iterations compared with **AE-PADMM** and **PC-PADMM**, but its relative error is relatively larger because of lacking heuristic approaches to handle integer optimization variables. **AE-PADMM** has a decent performance on solution optimality, but it is evidently computationally consuming due to the more complex iteration procedure involved. **PC-PADMM** balances the convergence rate and solution optimality well and has the best general performance.

4.5. Validation of the proposed nested distributed optimization

Sections 4.3 and 4.4 have respectively validated the distributed problem solving in the outer and inner iteration loops. We currently combine the improved GBD and ADMM to form the nested distributed optimization method. Particularly, for the outer iteration loop, we consider that the distributed agent of the RES#1 encounters the communication delay and this condition is consistent with **Scnr.II** mentioned in Section 4.3, and **A-MGBD** is employed (as described in Algorithm 1). For the inner iteration, according to the comparison results presented in Section 4.4, we select **PC-PADMM** (as described in Algorithm 3) considering it has the best general performance.

We define: (1) **DM**: Our developed nested distributed optimization method, which has the nested iteration loop. (2) **CM**: GBD with multi-cut generation, which has the single iteration loop, as the compared method, in Table 5. We would like to address that the iteration procedure in **CM** can be regarded as the benchmark for **DM**. This is because the outer iteration loop in **DM** is the same as **CM**. As the presented results in Table 5, it can be observed that **DM** has one more iteration compared with **CM**. Reviewing Tables 3 and 4, we can deduce that in each outer iteration, the distributed problem solving in MP has errors caused by **PC-PADMM**. Therefore, the iterations in **DM** and **CM** are inconsistent. Besides, the solution optimality is affected to some extent. However, **DM** is still competitive. The most prominent advantage of **DM** is the savings in communication costs. **DM** is considered to have lower communication costs compared to **CM**. This is because MP in **DM** is solved by distributed optimization instead of centralized optimization. The cumulative neighbor communication in distributed optimization often results in lower overall communication costs than the one-time but extensive communication required in centralized optimization. Besides, the sacrifice in the convergence rate and the solution optimality of **DM** is acceptable, considering just only one additional iteration and the increased absolute relative error of less than 0.20%. Particularly, Fig. 12 presents the inner iteration process at the last outer iteration. It can be seen that as the inner iterations increase, the residuals gradually decrease, and the augmented Lagrangian function of the inner PC-PADMM converges to a stable numerical value. This value serves as the *LB* of the optimization objective in the outer GBD as it converges.

We use Fig. 13 to illustrate the changes of boundary power at the PCC bus of VSC, which helps to better demonstrate the so-called "Nested" distributed optimization process. We can observe that each

Table 5
Comparison of distributed problem solving.

Description	Structure	Iter.	Obj.	Abs. Relative Err.
Cen.	–	–	1.7198	–
CM	Single loop	15	1.7201	0.0174%
DM	Outer & Inner loop	16 (Outer)	1.7231	0.1919%

iteration in the outer iteration loop contains a number of inner iterations. Specifically, the boundary power value observed during an outer iteration is the result of over a hundred inner iterations.

In addition, we conduct further numerical experiments based on larger-scale systems to comprehensively evaluate the performance of the proposed nested distributed optimization method. The detailed numerical results are provided in Appendix D. The obtained results demonstrate that the nested distributed optimization methods have the decent performances on the convergence rate and solution optimality. It can be concluded that the proposed nested distributed optimization method exhibits good scalability.

5. Conclusion

This paper introduces an enhanced AC/DC OPF via the nested distributed optimization, for achieving the coordinated operation for AC/VSC-MTDC hybrid power systems, fully relying on distributed communication. Through theoretical analysis and numerical experiments, we draw the following main conclusions.

- A series of linear approximation and convex relaxation techniques have been used to transform the original nonlinear AC/DC OPF model into the mixed-integer convex one. The resulting AC/DC OPF model has acceptable accuracy in terms of AC/DC power flow calculation and is compatible with the developed nested distributed optimization method, allowing for feasible decision making that adheres to the system-wide operational constraints.
- The inner iteration loop of the nested distributed optimization serves to coordinate the operation of AC systems and VSC-MTDC grid. The improved GBD, with multi-cut generation and asynchronous updating, shows good performance in solving the outer distributed problem. On one hand, it has a faster convergence rate compared to the standard GBD and can handle multiple SPs associated with the AC systems simultaneously without the need for a central coordinator. On the other hand, it also addresses the communication delay issues encountered during the cut-returning procedure.
- The outer iteration loop of the nested distributed optimization serves to coordinate the operation of multiple VSC areas within the VSC-MTDC grid. The improved ADMM, incorporating proximal terms and heuristic approaches, performs well in achieving parallel computation among sub-MPs associated with the VSC areas and handling the involved integer variables. Additionally, both the AOP procedure and penalty updating can be selected to handle the integer variables. Penalty updating is recommended, as it has the best general performance in terms of convergence rate and solution optimality.

It is acknowledged that there are certainly more advanced algorithm combinations that can exhibit better convergence rate and solution optimality. We will explore a more efficient nested distributed optimization method in future work. Furthermore, this work does not address the uncertainties from RESs, which would affect the decision making regarding the operation of AC/VSC-MTDC hybrid power systems. In future work, we will consider extending the enhance AC/DC OPF to incorporate distributionally robust optimization technique.

CRediT authorship contribution statement

Haixiao Li: Writing – original draft, Software, Methodology, Conceptualization. **Pedro P. Vergara:** Writing – review & editing. **Robert Dimitrovski:** Supervision, Funding acquisition. **Hongjin Du:** Conceptualization. **Aleksandra Lekić:** Writing – review & editing, Supervision, Funding acquisition, Conceptualization.

Declaration of competing interest

The authors declare that they have no known competing financial interests or personal relationships that could have appeared to influence the work reported in this paper.

Acknowledgments

This work was supported in part by the China Scholarship Council, China, and in part by CRESYM project Harmony (https://cresym.eu/harmony/).

Appendix A. Details regarding $g_{ij}^{P,init}$, $b_{ij}^{Q,init}$, $g_{ij}^{Q,init}$, $b_{ij}^{Q,init}$, $v_{ij}^{L,init}$

The specific formulations are listed below.

$$g_{ij}^{P,init} = \left(g_{ij}c_{ij}^{0,init} + b_{ij}s_{ij}^{0,init}\right) + \left(g_{ij}c_{ij}^{1,init} + b_{ij}s_{ij}^{1,init}\right)\theta_{ij}^{init}, \tag{A.1a}$$

$$b_{ij}^{P,init} = \left(g_{ij}c_{ij}^{1,init} + b_{ij}s_{ij}^{1,init}\right)v_i^{init}v_j^{init}, \tag{A.1b}$$

$$b_{ij}^{Q,init} = \left(-g_{ij}s_{ij}^{0,init} + b_{ij}c_{ij}^{0,init}\right) - \left(g_{ij}s_{ij}^{1,init} - b_{ij}c_{ij}^{1,init}\right)\theta_{ij}^{init}, \tag{A.1c}$$

$$g_{ij}^{Q,init} = \left(g_{ij}s_{ij}^{1,init} - b_{ij}c_{ij}^{1,init}\right)v_i^{init}v_j^{init}, \tag{A.1d}$$

where

$$s_{ij}^{1,init} = \cos\theta_{ij}^{init}, \quad s_{ij}^{0,init} = \sin\theta_{ij}^{init} - \theta_{ij}^{init}\cos\theta_{ij}^{init}, \tag{A.2a}$$

$$c_{ij}^{1,init} = -\sin\theta_{ij}^{init}, \quad c_{ij}^{0,init} = \cos\theta_{ij}^{init} + \theta_{ij}^{init}\sin\theta_{ij}^{init}. \tag{A.2b}$$

Appendix B. Additional numerical experiments regarding the optimization gap

The numerical experiments are done using the additional test systems shown in Fig. B.14. The AC grid is expanded to the larger scales, to 30 nodes, 57 nodes, and 89 nodes, respectively. The scale of the VSC-MTDC grid remains unchanged as a 4-terminal network, considering that in reality, VSC-MTDC systems typically have 3 to 5 terminals.

Simulation setups: The key parameters of VSC-MTDC grid and RESs are marked in Fig. B.14. The AC grid parameters originate from MATPOWER formats "case_ieee30", "case_57", and "case_89pegase". In "case_ieee30" and "case_57", the default parameter setting of branches does not include power capacity limits. In "case_89pegase", the default parameter setting of a part of branches does not include power capacity limits. Due to this reason, the branch power capacity constraint formulated by Eq. (5) is not considered in these additional test systems. The allowable deviation range of system-wide voltage is considered to be ±10% in additional test systems, and voltage bounds in the proposed mixed-integer convex AC/DC OPF model is set as $\underline{v_i} := 0.91$ p.u., $\overline{v_i} := 1.09$ p.u., $\forall i \in \mathbb{N}^{AC} \cup \mathbb{N}^{VSC} \cup \mathbb{N}^{MTDC}$. Additionally, the generator power output constraint formulated by Eq. (5) in the main text is modified to Eq. (B.1) below, considering in "case_ieee30", "case_ieee57", and "case_89pegase", the generator active and reactive power limits are given separately. Specifically, we are concerned about the possibility of no feasible power flow solutions. Therefore, the reactive power limits of generators in "case_ieee30", "case_57", and "case_89pegase" have been increased to 10 times of their original values. This means that the feasible region of the constructed AC/DC OPF problem has

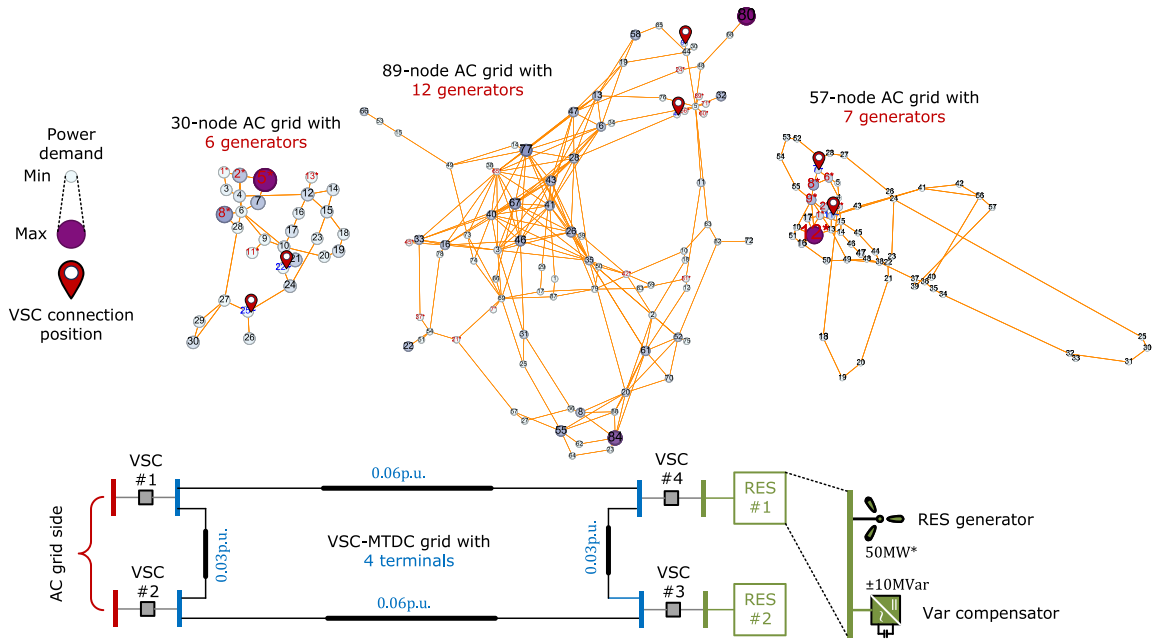

Fig. B.14. Schematic diagram of the additional test systems. The AC grids have three system scales, varying from 30 nodes to 89 nodes. The MTDC grid is a fixed 4-terminal network, with two nodes connected to the AC grid and the remaining two nodes connected to RESs. Case System I, II, and III refer to the AC/VSC-MTDC hybrid power system with 30-node AC grid, 57-node AC grid, and 89-node AC grid, respectively.

been expanded, and a feasible solution is more likely to exist. The remaining key settings are consistent with those in Section 4.1.

$$\underline{p^{AC}_{i,G}} \le p^{AC}_{i,G} \le \overline{p^{AC}_{i,G}}, \quad \underline{q^{AC}_{i,G}} \le q^{AC}_{i,G} \le \overline{q^{AC}_{i,G}}. \tag{B.1}$$

Comparison regarding the optimality gaps under different values of the adjustable parameters is made. For the proposed mixed-integer convex AC/DC OPF models, the adjustable parameters that influence linearization approximation and convex relaxation include: $\mathcal{N}_n$ in Eq. (12), $\mathcal{N}_k$ in Eq. (13), and $\mathcal{N}_k$ in Eq. (27). Their default values are set to $\mathcal{N}_n := 16$, $\mathcal{N}_k := 6$, and $\mathcal{N}_k := 2$. When performing sensitivity analysis on one of the mentioned adjustable parameters, the remaining parameters are kept at their default values. The optimization objectives of the proposed mixed-integer convex AC/DC OPF model under different values of adjustable parameters are shown in Tables B.6 to B.14. For the proposed OPF model, the optimization objectives are related to the initial AC power flow points. For a fair comparison, 5 updates regarding the initial AC power flow points are performed for each situation. The optimization objectives obtained from the original nonlinear AC/DC OPF model are regarded as the benchmark values. In the following discussion, we will use "approximated optimization objectives" to refer to the results obtained from the proposed OPF model, and "real optimization objectives" to refer to the benchmark values.

It can be found that as the number of updates increases, the approximated optimization objective gradually converges to a stable value, closely approaching the real optimization objective. In terms of optimality, the proposed OPF model has a decent performance. Also, we notice that the selected values of the adjustable parameters do not significantly impact the converged optimization objective, based solely on the numerical results from the test systems. Moreover, due to the adoption of various convex relaxation techniques in the proposed OPF model, the feasible region of the OPF solution is expanded, and the approximated optimization objective should be less than the real optimization objective. However, influenced by the successive linearization technique applied in the AC grid, along with more conservative voltage bound settings ($0.91 \sim 1.09$ p.u.), the feasible region does not necessarily be expanded. As a consequence, the approximated optimization objectives are slightly greater than the real optimization objectives for all case systems.

Appendix C. Additional numerical experiments regarding the power flow calculation

We use the additional test systems in Fig. B.14 to verify the accuracy of the proposed OPF model in power flow calculations. As a result, we obtain the results regarding the accuracy of power flow solutions as shown in Tables C.15 to C.17 (has gone through 5 updates of the AC initial power flow points). We can see that under the default parameters settings, the proposed mixed-integer convex AC/DC OPF model exhibits acceptable accuracy in terms of power flow solutions. The maximum calculation error in node voltage is much smaller than 0.01 p.u. and the maximum calculation error in power flow(active) is also much smaller than 2% of the total power demands(active). As $\mathcal{N}_n$ increases, it is intuitive that the approximation of the nonlinear RES power output constraints using Eq. (12) improves. As $\mathcal{N}_k$ increases, it is intuitive that the convex envelopes formed by Eq. (24) and (27) tightens. However, this does not necessarily lead to an increase in the accuracy of the system-wide power flow calculations. This is because the selection of $\mathcal{N}_n$ in Eq. (12), $\mathcal{N}_k$ in Eq. (24), and $\mathcal{N}_k$ in Eq. (27), will lead to different initial AC power flow points, which also significantly influence the accuracy of power flow calculations.

We can conclude that for the proposed OPF model, the sensitivities of power flow calculation accuracy to the mentioned adjustable parameters are relatively weak. Moreover, based on the default parameter settings, the accuracy of power flow calculations for all test systems is acceptable.

Appendix D. Additional numerical experiments regarding the nested distributed optimization

We use the additional test systems with larger scales to further validate the scalability of the proposed nested distributed optimization method. We would like to note that the threshold in the outer iteration loop is relaxed to 5×10^{-3} to account the increase in optimization problem size, which is likely to lead the slower reduction in the gap between UB and LB. A relatively relaxed threshold can achieve a better trade-off between convergence rate and solution optimality. The threshold and maximum iteration number in the inner iteration loop

Table B.6
Optimization objectives with different $\mathcal{N}_n^{\wedge}$ in Eq. (12) for Case System I.

$\mathcal{N}_n^{\wedge}$	Obj. in the proposed mixed-integer convex OPF model [–]					Obj. in the nonlinear OPF model [–]
	1st updates	2nd updates	3rd updates	4th updates	5th updates	
8	5.0918	5.5027	5.5066	5.5066	5.5066	5.5036
16	5.0918	5.5028	5.5066	5.5066	5.5066	
32	5.0918	5.5028	5.5066	5.5066	5.5066	
40	5.0918	5.5026	5.5066	5.5066	5.5066	

Table B.7
Optimization objectives with different $\mathcal{N}_k^{\wedge}$ in Eq. (24) for Case System I.

$\mathcal{N}_k^{\wedge}$	Obj. in the proposed mixed-integer convex OPF model [–]					Obj. in the nonlinear OPF model [–]
	1st updates	2nd updates	3rd updates	4th updates	5th updates	
4	5.0914	5.5026	5.5065	5.5065	5.5064	5.5036
6	5.0918	5.5028	5.5066	5.5066	5.5066	
8	5.0918	5.5028	5.5066	5.5066	5.5066	
10	5.0918	5.5027	5.5029	5.5066	5.5066	

Table B.8
Optimization objectives with different $\mathcal{N}_k^{\wedge}$ in Eq. (27) for Case System I.

$\mathcal{N}_k^{\wedge}$	Obj. in the proposed mixed-integer convex OPF model [–]					Obj. in the nonlinear OPF model [–]
	1st updates	2nd updates	3rd updates	4th updates	5th updates	
1	5.0917	5.5027	5.5066	5.5066	5.5066	5.5036
2	5.0918	5.5028	5.5066	5.5066	5.5066	
3	5.0918	5.5028	5.5066	5.5066	5.5065	
5	5.0918	5.5028	5.5063	5.5066	5.5066	

Table B.9
Optimization objectives with different $\mathcal{N}_n^{\wedge}$ in Eq. (12) for Case System II.

$\mathcal{N}_n^{\wedge}$	Obj. in the proposed mixed-integer convex OPF model [–]					Obj. in the nonlinear OPF model [–]
	1st updates	2nd updates	3rd updates	4th updates	5th updates	
8	47.1329	47.7196	47.7198	47.7198	47.7198	47.6936
16	47.1329	47.7196	47.7198	47.7198	47.7197	
32	47.1329	47.7197	47.7197	47.7197	47.7198	
40	47.1329	47.7197	47.7197	47.7197	47.7198	

Table B.10
Optimization objectives with different $\mathcal{N}_k^{\wedge}$ in Eq. (24) for Case System II.

$\mathcal{N}_k^{\wedge}$	Obj. in the proposed mixed-integer convex OPF model [–]					Obj. in the nonlinear OPF model [–]
	1st updates	2nd updates	3rd updates	4th updates	5th updates	
4	47.1325	47.7192	47.7195	47.7193	47.7195	47.6936
6	47.1329	47.7196	47.7198	47.7198	47.7197	
8	47.1331	47.7198	47.7200	47.7199	47.7200	
10	47.1332	47.7199	47.7201	47.7201	47.7199	

Table B.11
Optimization objectives with different $\mathcal{N}_k^{\wedge}$ in Eq. (27) for Case System II.

$\mathcal{N}_k^{\wedge}$	Obj. in the proposed mixed-integer convex OPF model [–]					Obj. in the nonlinear OPF model [–]
	1st updates	2nd updates	3rd updates	4th updates	5th updates	
1	47.1329	47.7198	47.7198	47.7199	47.7198	47.6936
2	47.1329	47.7196	47.7198	47.7198	47.7197	
3	47.1329	47.7197	47.7198	47.7198	47.7199	
5	47.1329	47.7198	47.7199	47.7197	47.7197	

remain unchanged, as 1×10^{-3} and 250, respectively. Communication delay scenario **Scnr.II** is still taken into account.

The obtained problem-solving results are shown in Table D.18. We can see that the outer iteration number of the proposed nested distributed optimization method (represented by **DM**) is still close to the iteration number of MGBD (represented by **CM**). Additionally, the converged optimization objectives closely approach those of the centralized optimization. Hence, we can conclude that the proposed nested distributed optimization method still has the decent performances on convergence rate and solution optimality when applied to larger-scale systems, demonstrating good scalability.

In particular, we present the nested iteration optimization procedure in Case System II. Fig. D.15 illustrates the corresponding nested distributed optimization process from the perspective of *LB*, which is obtained by solving MP, hence, changes in both outer and inner

Table B.12
Optimization objectives with different $\mathcal{N}_n$ in Eq. (12) for Case System III.

$\mathcal{N}_n$	Obj. in the proposed mixed-integer convex OPF model [–]					Obj. in the nonlinear OPF model [–]
	1st updates	2nd updates	3rd updates	4th updates	5th updates	
8	537.7070	524.5826	524.0986	524.0961	524.1187	524.0596
16	537.7070	524.5828	524.0993	524.0959	524.0968	
32	537.7072	524.5825	524.0982	524.0954	524.0965	
40	537.7072	524.5824	524.0986	524.0964	524.0960	

Table B.13
Optimization objectives with different $\mathcal{N}_k$ in Eq. (24) for Case System III.

$\mathcal{N}_k$	Obj. in the proposed mixed-integer convex OPF model [–]					Obj. in the nonlinear OPF model [–]
	1st updates	2nd updates	3rd updates	4th updates	5th updates	
4	537.7065	524.0950	524.0955	524.0956	524.0956	524.0596
6	537.7070	524.5828	524.0993	524.0959	524.0968	
8	537.7070	524.5826	524.0981	524.0951	524.0955	
10	537.7073	524.5832	524.0993	524.0956	524.0955	

Table B.14
Optimization objectives with different $\mathcal{N}_k$ in Eq. (27) for Case System III.

$\mathcal{N}_k$	Obj. in the proposed mixed-integer convex OPF model [–]					Obj. in the nonlinear OPF model [–]
	1st updates	2nd updates	3rd updates	4th updates	5th updates	
1	537.7064	524.5828	524.0982	524.0950	524.0961	524.0596
2	537.7070	524.5828	524.0993	524.0959	524.0968	
3	537.7070	524.5836	524.0986	524.0957	524.0951	
5	537.7078	524.5825	524.0981	524.0957	524.0952	

Table C.15
Accuracy of power flow solutions with different $\mathcal{N}_n$ in Eq. (12).

$\mathcal{N}_n$	Calculation errors in Case System I		Calculation errors in Case System II		Calculation errors in Case System III	
	Node voltage [p.u.] Max./Ave.	Power flow [MW] Max./Ave.	Node voltage [p.u.] Max./Ave.	Power flow [MW] Max./Ave.	Node voltage [p.u.] Max./Ave.	Power flow [MW] Max./Ave.
8	1.1226E−3/2.6454E−4	3.3612/0.5072	6.9768E−4/1.6893E−4	1.0547/0.1028	2.5886E−3/7.7907E−5	10.3462/0.2707
16	1.2078E−3/2.7384E−4	3.3694/0.5087	6.9670E−4/1.6913E−4	0.9149/0.0897	3.3374E−3/1.5098E−4	7.5107/0.2002
32	1.111E−3/2.6534E−4	3.3083/0.4992	6.8729E−4/1.6683E−4	0.9270/0.0908	1.5488E−3/8.8714E−5	7.4806/0.1947
40	1.0792E−3/2.6144E−4	3.2895/0.4962	6.9461E−4/1.6913E−4	0.9063/0.0888	8.9449E−4/3.3032E−5	1.0404/0.0273

Table C.16
Accuracy of power flow solutions with different $\mathcal{N}_k$ in Eq. (24).

$\mathcal{N}_k$	Calculation errors in Case System I		Calculation errors in Case System II		Calculation errors in Case System III	
	Node voltage [p.u.] Max./Ave	Power flow [MW] Max./Ave.	Node voltage [p.u.] Max./Ave.	Power flow [MW] Max./Ave.	Node voltage [p.u.] Max./Ave.	Power flow [MW] Max./Ave.
4	1.0267E−3/2.5620E−4	3.2772/0.4944	6.9448E−4/1.6896E−4	0.9084/0.0892	2.1623E−3/1.5723E−4	6.5653/0.2196
6	1.2078E−3/2.7384E−4	3.3694/0.5087	6.9670E−4/1.6913E−4	0.9149/0.0897	3.3374E−3/1.5098E−4	7.5107/0.2002
8	1.111E−3/2.7277E−4	3.2914/0.4969	6.9186E−4/1.6785E−4	0.9071/0.0889	1.4972E−3/1.0514E−4	4.1368/0.1153
10	1.0278E−3/2.4231E−4	3.2807/0.4938	8.6504E−4/2.0809E−4	1.0981/0.1078	3.4758E−4/1.5458E−4	10.3099/0.2748

Table C.17
Accuracy of power flow solutions with different $\mathcal{N}_k$ in Eq. (27).

$\mathcal{N}_k$	Calculation errors in Case System I		Calculation errors in Case System II		Calculation errors in Case System III	
	Node voltage [p.u.] Max./Ave	Power flow [MW] Max./Ave	Node voltage [p.u.] Max./Ave	Power flow [MW] Max./Ave.	Node voltage [p.u.] Max./Ave.	Power flow [MW] Max./Ave.
1	1.0721E−3/2.6052E−4	3.3060/0.4988	7.2105E−4/1.7441E−4	0.9742/0.0954	3.1200E−3/1.2117E−4	7.2766/0.1927
2	1.2078E−3/2.7384E−4	3.3694/0.5087	6.9670E−4/1.6913E−4	0.9149/0.0897	3.3374E−3/1.5098E−4	7.5107/0.2002
3	1.0692E−3/2.6063E−4	3.2868/0.4966	6.9204E−4/1.6807E−4	0.9040/0.0886	2.8239E−3/1.3656E−4	4.5111/0.1210
5	1.0741E−3/2.6053E−4	3.2746/0.4940	6.7896E−4/1.6518E−4	0.9071/0.0888	3.2887E−4/1.4093E−4	7.7870/0.2072

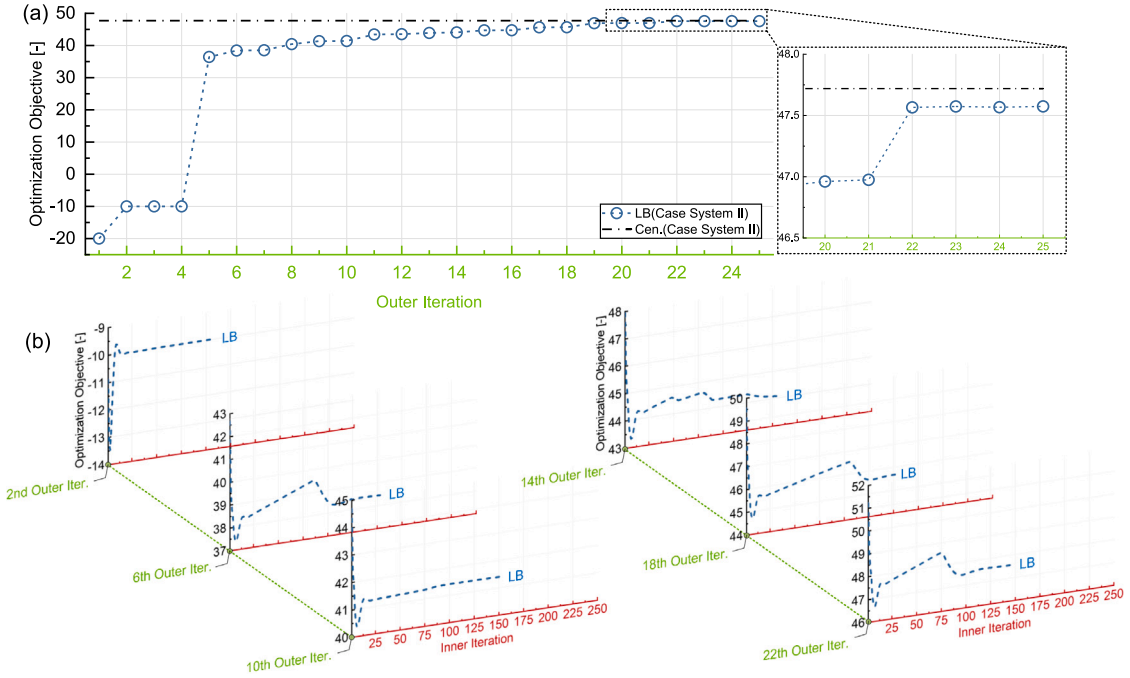

Fig. D.15. Changes of *LB* during the outer and inner iteration loops. (a) shows the change of *LB* during the outer iteration loop. (b) shows the change of *LB* during the inner iteration loop.

Table D.18
Comparison of distributed problem solving in additional case systems.

Case System	CM		DM		Cen.
	Iter.	Obj.	Outer Iter.	Obj.	Obj.
I	21	5.5002	23	5.5087	5.5066
II	23	47.6687	25	47.6888	47.7197
III	14	524.3872	14	524.3014	524.0954

iterations. It can be observed that *LB* converges successfully in both inner and outer iteration loops.

Data availability

Data will be made available on request.

References

[1] Vehlow C, Reinhardt T, Weiskopf D. HVDC transmission: Technology review, market trends and future outlook. Renew Sustain Energy Rev 2019 112:530–54.

[2] Xue Y, Zhang X-P. Near linear time algorithm to detect community structures in large-scale networks. IEEE Trans Power Syst 2016;32:753–64.

[3] Shah R, Sánchez JC, Preece R, Barnes M. Stability and control of mixed AC–DC systems with VSC-HVDC: a review. IET Gener Transm Distrib 2018;12:2207–19.

[4] Guo L, Ding Y, Bao M, Shao C, Wang P, Goel L. Nodal reliability evaluation for a VSC-MTDC-based hybrid AC/DC power system. IEEE Trans Power Syst 2019;35:2300–12.

[5] Feng W, Tjernberg LB, Mannikoff A, Bergman A, et al. A new approach for benefit evaluation of multiterminal VSC–HVDC using a proposed mixed AC/DC optimal power flow. IEEE Trans Power Deliv 2013;29:432–43.

[6] Daelemans G, Srivastava K, Reza M, Cole S, Belmans R. Minimization of steady-state losses in meshed networks using VSC HVDC. In: 2009 IEEE power & energy society general meeting. IEEE; 2009, p. 1–5.

[7] Liao C, Tan Y, Li Y, Cao Y. Optimal operation for hybrid AC and DC systems considering branch switching and VSC control. IEEE Syst J 2022;16:6708–16.

[8] Huang Z, Zhu T, Gu Y, Li Y. Shepherd: sharing energy for privacy preserving in hybrid AC-DC microgrids. In: Proceedings of the seventh international conference on future energy systems. 2016, p. 1–10.

[9] Geoffrion AM. Generalized benders decomposition. J Optim Theory Appl 1972;10(4):237–60.

[10] Boyd S, Parikh N, Chu E, Peleato B, Eckstein J, et al. Distributed optimization and statistical learning via the alternating direction method of multipliers. Found Trends® Mach Learn 2011;3:1–122.

[11] Hui Q, Teng Y, Zuo H, Chen Z. Reactive power multi-objective optimization for multi-terminal AC/DC interconnected power systems under wind power fluctuation. CSEE J Power Energy Syst 2019;6:630–7.

[12] Beg F. Interior point algorithm-based power flow optimisation of a combined AC and DC multi-terminal grid. J Eng 2015;2015:41–7.

[13] Zhang H, Heydt GT, Vittal V, Quintero J. An improved network model for transmission expansion planning considering reactive power and network losses. IEEE Trans Power Syst 2013;28:3471–9.

[14] Yang Z, Zhong H, Xia Q, Bose A, Kang C. Optimal power flow based on successive linear approximation of power flow equations. IET Gener Transm Distrib 2016;10:3654–62.

[15] Yang Z, Zhong H, Bose A, Zheng T, Xia Q, Kang C. A linearized OPF model with reactive power and voltage magnitude: A pathway to improve the MW-only DC OPF. IEEE Trans Power Syst 2017;33:1734–45.

[16] Montoya OD, Grisales-Noreña L, González-Montoya D, Ramos-Paja C, Garces A. Linear power flow formulation for low-voltage DC power grids. Electr Power Syst Res 2018;163:375–81.

[17] Montoya OD. On linear analysis of the power flow equations for DC and AC grids with CPLs. IEEE Trans Circuits Syst II 2019;66:2032–6.

[18] Bai X, Wei H, Fujisawa K, Wang Y. Semidefinite programming for optimal power flow problems. Int J Electr Power Energy Syst 2008;30:383–92.

[19] Coffrin C, Hijazi HL, Van Hentenryck P. The QC relaxation: A theoretical and computational study on optimal power flow. IEEE Trans Power Syst 2015;31:3008–18.

[20] Kocuk B, Dey SS, Sun XA. Strong SOCP relaxations for the optimal power flow problem. Oper Res 2016;64:1177–96.

[21] Gan L, Low SH. Optimal power flow in direct current networks. IEEE Trans Power Syst 2014;29:2892–904.

[22] Ergun H, Dave J, Van Hertem D, Geth F. Optimal power flow for AC–DC grids: Formulation, convex relaxation, linear approximation, and implementation. IEEE Trans Power Syst 2019;34(4):2980–90.

[23] Castro PM. Tightening piecewise McCormick relaxations for bilinear problems. Comput Chem Eng 2015;72:300–11.

[24] Hijazi H, Coffrin C, Hentenryck PV. Convex quadratic relaxations for mixed-integer nonlinear programs in power systems. Math Program Comput 2017;9:321–67.

[25] Cohen G. Auxiliary problem principle and decomposition of optimization problems. J Optim Theory Appl 1980;32:277–305.

[26] Zhang G, Heusdens R. Distributed optimization using the primal-dual method of multipliers. IEEE Trans Signal Inf Process Netw 2017;4(1):173–87.

[27] Engelmann A, Jiang Y, Mühlpfordt T, Houska B, Faulwasser T. Toward distributed OPF using ALADIN. IEEE Trans Power Syst 2018;34(1):584–94.

[28] Meyer-Huebner N, Suriyah M, Leibfried T. Distributed optimal power flow in hybrid AC–DC grids. IEEE Trans Power Syst 2019;34(4):2937–46.
[29] Zhai J, Dai X, Jiang Y, Xue Y, Hagenmeyer V, Jones CN, Zhang X-P. Distributed optimal power flow for VSC-MTDC meshed AC/DC grids using ALADIN. IEEE Trans Power Syst 2022;37(6):4861–73.
[30] Jiang Z, Liu Y, Kang Z, Han T, Zhou J. Security-constrained unit commitment for hybrid VSC-MTDC/AC power systems with high penetration of wind generation. IEEE Access 2022;10:14029–37.
[31] Altun T, Madani R, Davoudi A. Topology-cognizant optimal power flow in multi-terminal DC grids. IEEE Trans Power Syst 2021;36:4588–98.
[32] Li H, Lekić A. Distributed robust optimization method for AC/MTDC hybrid power systems with DC network cognizant. In: 2024 international conference on smart energy systems and technologies. SEST, 2024, p. 1–6.
[33] Feng W, Shi Q, Cui H, Li F, Yuan C, Dai R, Liu G. Using Lagrangian relaxation to include operating limits of VSC-MTDC system for state estimation. In: 2020 IEEE power & energy society general meeting. PESGM, IEEE; 2020, p. 1–5.
[34] Aziz S, Peng J, Wang H, Jiang H. Admm-based distributed optimization of hybrid mtdc-ac grid for determining smooth operation point. IEEE Access 2019;7:74238–47.
[35] Chen X, Zhai J, Shen J, Wang Q, Li S, Wang S. Distributed and distributionally robust chance-constrained scheduling for VSC-MTDC meshed AC/DC power networks. IEEE Trans Netw Sci Eng 2024.
[36] Mohamed MA, Abdullah HM, Al-Sumaiti AS, El-Meligy MA, Sharaf M, Soliman AT. Towards energy management negotiation between distributed AC/DC networks. IEEE Access 2020;8:215438–56.
[37] Zhang S, Zhou M, Liu Z, Li G, Zhang L. Hierarchical flexible operation approach on a VSC-MTDC interconnected hybrid grid with a high share of renewable power. IEEE Trans Power Syst 2022;37:4936–49.
[38] Zhai J, Zhou M, Li J, Zhang X-P, Li G, Ni C, Zhang W. Hierarchical and robust scheduling approach for VSC-MTDC meshed AC/DC grid with high share of wind power. IEEE Trans Power Syst 2020;36:793–805.
[39] Inaolaji A, Savasci A, Paudyal S. Distribution grid optimal power flow in unbalanced multiphase networks with volt-var and volt-watt droop settings of smart inverters. IEEE Trans Ind Appl 2022;58:5832–43.
[40] Li H, Lekić A, Li S, Jiang D, Guo Q, Zhou L. Distribution network reconfiguration considering the impacts of local renewable generation and external power grid. IEEE Trans Ind Appl 2023;59(6):7771–88.
[41] Li H, Guo K, Hao G, Mao M, Zhou L. Decentralized communication based two-tier volt-var control strategy for large-scale centralized photovoltaic power plant. IEEE Trans Sustain Energy 2021;13:592–606.
[42] Kim T, Song J, You D. Optimization of a wind farm layout to mitigate the wind power intermittency. Appl Energy 2024;367:123383.
[43] de Araujo RA, Torres SP, Pissolato Filho J, Castro CA, Van Hertem D. Unified AC transmission expansion planning formulation incorporating VSC-MTDC, FACTS devices, and reactive power compensation. Electr Power Syst Res 2023;216:109017.
[44] Cao Y, Wang W, Li Y, Tan Y, Chen C, He L, Häger U, Rehtanz C. A virtual synchronous generator control strategy for VSC-MTDC systems. IEEE Trans Energy Convers 2017;33:750–61.
[45] Shen L, Barnes M, Preece R, Milanovic JV, Bell K, Belivanis M. The effect of VSC-HVDC control on AC system electromechanical oscillations and DC system dynamics. IEEE Trans Power Deliv 2015;31:1085–95.
[46] You F, Grossmann IE. Multicut benders decomposition algorithm for process supply chain planning under uncertainty. Ann Oper Res 2013;210:191–211.
[47] Yang Y, Jia Q-S, Xu Z, Guan X, Spanos CJ. Proximal admm for nonconvex and nonsmooth optimization. Automatica 2022;146:110551.
[48] Hong M, Luo Z-Q, Razaviyayn M. Convergence analysis of alternating direction method of multipliers for a family of nonconvex problems. SIAM J Optim 2016;26(1):337–64.
[49] Li P, Zhang C, Wu Z, Xu Y, Hu M, Dong Z. Distributed adaptive robust voltage/var control with network partition in active distribution networks. IEEE Trans Smart Grid 2019;11(3):2245–56.
[50] Wuijts RH, Akker Mvd, Broek Mvd. New efficient ADMM algorithm for the unit commitment problem. 2023, arXiv preprint arXiv:2311.13438.